On the benefits of road preview on integrated chassis control

Taylor & Francis
Taylor & Francis Group

Vehicle System Dynamics

International Journal of Vehicle Mechanics and Mobility

ISSN: 0042-3114 (Print) 1744-5159 (Online) Journal homepage: www.tandfonline.com/journals/nvsd20

On the benefits of road preview on integrated chassis control

Davide Lazzarini, Matteo Depalo, Antonio Tota, Luca Dimauro, Miguel Dhaens & Aldo Sorniotti

To cite this article: Davide Lazzarini, Matteo Depalo, Antonio Tota, Luca Dimauro, Miguel Dhaens & Aldo Sorniotti (01 Apr 2026): On the benefits of road preview on integrated chassis control, Vehicle System Dynamics, DOI: 10.1080/00423114.2026.2634102

To link to this article: https://doi.org/10.1080/00423114.2026.2634102

Published online: 01 Apr 2026.

VEHICLE SYSTEM DYNAMICS
https://doi.org/10.1080/00423114.2026.2634102

On the benefits of road preview on integrated chassis control

Davide Lazzarini [a], Matteo Depalo[a], Antonio Tota[a], Luca Dimauro[a], Miguel Dhaens[b] and Aldo Sorniotti [a]

[a]Department of Mechanical and Aerospace Engineering (DIMEAS), Politecnico di Torino, Turin, Italy; [b]Research and Development, HERONSports, Lommel, Belgium

ABSTRACT

Integrated chassis controllers (ICCs), which are based on the coordinated or unified control of multiple vehicle dynamics actuators, are likely to benefit from vehicle-to-everything communication, advanced sensors, sensor fusion, and driving automation. In fact, such techniques anticipate information that can increase prediction accuracy and performance of model-based vehicle dynamics controllers. Although a few publications have explored road-preview-based vehicle dynamics control, there is a gap in terms of a critical assessment of the benefits of ICCs with different levels of preview. This preliminary proof-of-concept study analyses the potential advantage of a set of road preview variables provided to nonlinear model predictive controllers (NMPCs) for integrated torque-vectoring and front-to-total anti-roll moment distribution. In addition to the commonly adopted steering input preview, multiple preview combinations are implemented, e.g. on the longitudinal and lateral accelerations, as well as on the tyre-road friction factors. The sensitivity analyses, using an experimentally validated high-fidelity vehicle model and optimised control tunings, cover the benefit of each source of preview, while considering the effects of (i) actuation dynamics, (ii) prediction horizon and (iii) level of mismatch of the preview information.

ARTICLE HISTORY
Received 2 June 2025
Revised 1 February 2026
Accepted 8 February 2026

KEYWORDS
Integrated chassis control; road preview; preview variables; nonlinear model predictive control; actuation dynamics; optimised control tuning

1. Introduction

In the last few decades, ICCs, which are based on the coordinated or unified control of multiple chassis actuators, have been proposed for a wide range of vehicle applications and objectives, including active safety, energy efficiency and ride comfort. Different integration levels are available [1], ranging from peaceful coexistence to centralised architectures. With respect to (w.r.t.) the latter, model predictive control (MPC), including its nonlinear form, is widely discussed in the recent literature, thanks to the progress in terms of control hardware and computationally efficient solvers [2,3], which are enabling real-time implementations at the low time steps required by ICC applications.

In the ICC context, a frequent actuation method is represented by torque-vectoring (TV) [4], which modifies the torque distribution among the wheels to improve vehicle stability and handling, e.g. by varying the level of understeer and increasing yaw and sideslip

CONTACT Aldo Sorniotti aldo.sorniotti@polito.it

damping, and in some cases to concurrently reduce the relevant power losses [5–12]. In electric vehicles (EVs), TV can be implemented through in-wheel machines (IWMs) or on-board powertrains. Although electric machines (EMs) are generally characterised by more accurate and fast torque dynamics than internal combustion engines, which facilitates TV operation, their dynamic response has large variability, depending on the specific EM.

Active suspension systems (ASSs) are another widely discussed chassis actuation method [13]. They are usually adopted for (a) vehicle body control, i.e. to manage the roll, pitch and heave dynamics induced by the driving actions or uneven road surfaces [14–19], and (b) road holding control [20–23], i.e. to reduce the dynamic tyre load caused by road irregularities. A further ASS functionality is represented by the anti-roll moment distribution (ARMD) variation between the front and rear axles [24,25], which, in the nonlinear cornering range, can control the level of understeer, similarly to TV. Given the nonlinearity of the involved lateral force behaviour, recent studies propose dedicated control-oriented models for ARMD [26]. The literature includes examples [27–29] of integrated TV and ARMD control, among which reference [5] proposes a centralised NMPC, targeting yaw rate tracking, powertrain and tyre slip power loss reduction, as well as longitudinal and lateral tyre slip limitation.

Traditionally, MPC implementations for vehicle dynamics control consider constant steering angle and traction/braking force demand along the prediction horizon, which limits prediction accuracy in the highly dynamic scenarios relevant to ICC. Hence, with such significant limitations, the MPC benefits are restricted to (a) the capability of achieving trade-offs among different complex objectives, (b) the possibility of formally embedding constraints and (c) adaptations to system parameter variations, facilitated by the model-based nature of MPC.

With the transition towards driving automation, ICC can be implemented either through: (i) centralised path tracking controllers, which, based on the tracking errors w.r.t. the reference trajectory, concurrently generate all the control inputs, i.e. in terms of front steering demand and reference values for the other chassis actuators [30], or (ii) multi-layer architectures, e.g. with a path tracking layer that is responsible for the control of the front steering angle and total vehicle torque demand, and lower layers that manage the other actuators, e.g. with yaw rate tracking and sideslip angle limitation objectives [31–32]. In both cases:

- Trajectory tracking is increasingly realised with MPC algorithms, which predict the future system dynamics and optimise the control inputs accordingly [33].
- Thanks to the presence of exteroceptive sensors, information on the road ahead, e.g. in terms of curvature, is available, which can be augmented by vehicle-to-everything (V2X) inputs [34], e.g. on the tyre-road friction level ahead.
- The expected steering and total torque demand profiles are known to the ICC system, since in option (i), they are computed concurrently with the ICC actions, while in (ii), they are available from the path tracking layer of the control architecture.

Hence, next-generation ICCs can become proactive rather than reactive. A few researchers have investigated chassis controllers that benefit from preview information. For example, reference [35] reviews the topic of preview-based suspension control to enhance

ride comfort, without any coverage in terms of cornering response benefits, which are the focus of this paper. The studies in ref. [36] and refs. [37–38] explore the benefits of the tyre-road friction level preview for anti-lock braking system (ABS) and traction control applications. However, only the longitudinal vehicle dynamics are considered, and the previews on the steering wheel angle or lateral vehicle dynamics are not included. Reference [39] proposes pre-emptive vehicle stability controllers that consider the curvature profile of the path ahead in the computation of the reference direct yaw moment and braking control action. The tyre-road friction factor and vehicle accelerations are included in the preview. However, the results focus on the pre-emptive braking effect, which appropriately slows down the vehicle in a straight line before entering the critical part of the test involving steering, while the analysis does not concentrate on the preview benefits that occur in the cornering phases. In ref. [40], Yim adopts linear quadratic static output feedback for rollover prevention through direct yaw moment and ASS control and considers the previewed steering input as a disturbance. In ref. [41], vehicle-to-vehicle (V2 V) communication is used to preview the steering profile of the ego vehicle based on one of the preceding vehicles, which is provided to a linear quadratic regulator for stability control through direct yaw moment and ASS actuation. Despite their high relevance, the linear quadratic approaches in refs. [40,41] do not represent the state-of-the-art for advanced vehicle control in limit handling conditions any longer, since the most recent NMPCs provide performance benefits, e.g. in terms of prediction of the nonlinear system dynamics and formal consideration of constraints. In ref. [42], Amer et al. preliminarily assess the improvement that steering angle preview can bring to two NMPC configurations for integrated TV and front-to-total (F2T) ARMD control, but also in this case, there is no discussion of the effect of introducing different preview signals. In ref. [43], Peenze et al. present a steering preview method applied to an off-road vehicle with semi-active suspensions, rear-wheel-steering and differential braking. Although a comparison of preview-based control algorithms is presented, the analysis remains limited to steering preview. Among the studies for automated vehicle applications, reference [44] discusses an MPC-based path tracking architecture with adaptive preview characteristics of the reference states, but the control inputs are limited to the front steering angle, tandem master cylinder pressure and accelerator demand. In ref. [45], within a multi-layer architecture, Ahn et al. integrate an autonomous driving control system with a chassis controller. The latter is responsible for adjusting the front steering and motor torque levels, while considering, on top of conventional yaw rate tracking, the preview information on the lateral position error predicted by the driving automation layer. In ref. [46], an upper-level path tracking MPC algorithm generates the reference front steering angle and direct yaw moment, which is provided as preview information to lower-level algorithms. In refs. [44–46], the respective chassis controllers rely on preview information from the path tracking algorithm but do not consider the tyre-road friction or acceleration previews.

In summary, although the ICC literature includes architectures with preview implementation examples, none of the available studies provide a systematic assessment of the benefits associated with each individual preview variable, such as the steering angle, longitudinal and lateral accelerations, or tyre-road friction level. While the benefits of steering input preview have been demonstrated, the role of the other preview variables relevant to the lateral dynamics remains insufficiently investigated. For example, the lateral and longitudinal acceleration preview could improve the wheel load prediction, which can be

Table 1. Main vehicle parameters in nominal conditions.

Description	Symbol	Value	Unit
Total vehicle mass	m	2843	[kg]
Front semi-wheelbase	a_f	1.473	[m]
Rear semi-wheelbase	a_r	1.455	[m]
Front and rear track width	$b_{f/r}$	1.655	[m]
Centre of gravity height	h_{CG}	0.631	[m]
Roll centre height (average for the front and rear suspensions)	h_{RC}	0.088	[m]
Wheel radius	R_w	0.37	[m]
Steering ratio	t_δ	0.06	[-]
Yaw mass moment of inertia	J_z	5291	[kgm^2]
Wheel mass moment of inertia	J_w	1.62	[kgm^2]
Active suspension force actuation time constant	τ_{as}	0.05	[s]
Electric motor torque actuation time constant	τ_{em}	0.02	[s]
Clamping force actuation time constant of the friction brakes	τ_{bk}	0.03	[s]

crucial, especially in the presence of active suspension actuation. Likewise, by previewing the tyre-road friction conditions and especially their abrupt variations from high to low levels, the controller could limit excessive wheel slip, and thereby preserve the lateral force capacity.

To address the gap, for an integrated TV and ASS NMPC implementation, this study brings the following novel contributions:

- The objective simulation-based comparison of preview information setups along multiple scenarios, involving extreme lateral and longitudinal vehicle dynamics, with constant and variable tyre-road friction. The analysis covers (a) vehicle configurations with different dynamic capabilities of the chassis actuators, (b) controllers that neglect or consider the chassis actuation dynamics and (c) sensitivities to the effect of error injections on the preview variables.
- The open-loop adoption of the NMPC prediction model to leverage the predicted vehicle states and expected tyre-road friction profile to obtain the preview information on the longitudinal and lateral accelerations, and thus, the respective load transfers.

The ambition is to provide preliminary high-level design guidelines for next-generation preview-based ICCs, without limiting the scope to real-time implementable solutions with currently available control hardware, or to specific sensing systems and state or parameter estimation setups, since all the mentioned technologies are expected to experience significant progress in the near future.

2. Simulation environment and control architecture

The case study EV is the prototype of the European Horizon 2020 EVC1000 project. Each vehicle corner is equipped with three actuators: (i) a direct drive IWM; (ii) a brake-by-wire actuator, based on electro-hydraulic (on the front axle) or electro-mechanical (on the rear axle) technology and (iii) an electro-hydraulic suspension system prototype, designed for roll angle compensation and F2T ARMD control, see [24]. The main vehicle parameters are in Table 1.

The simulation and control environment (Figure 1) consists of the following blocks, where (3)–(8) represent the ICC implementation:

(1) The tyre-road friction profile generator, which outputs the tyre-road friction factor μ_i (considered to be the same on the left and right corners of the same axle) as a function of time, ensuring independence from the vehicle's position, which could otherwise affect the evaluation of the controller's performance. Here and in the remainder, the subscript i, with $i = f, r$, refers to the front or rear axle, while the subscript j, with $j = l, r$, refers to the left or right vehicle side.
(2) The steering and pedal modules, providing the driver inputs in terms of accelerator and brake pedal displacements, p_a and p_b, and steering wheel angle, δ_{sw}, at the current time step.
(3) The preview module, providing the preview vectors on the tyre-road friction factor, $\bar{\mu}_i$, the steering wheel angle, $\bar{\delta}_{sw}$, the longitudinal and lateral accelerations, $\bar{a}_x$ and $\bar{a}_y$, and the reference yaw rate, $\overline{\dot{\psi}}_{ref}$. The latter is calculated through the interpolation of a nonlinear map, as a function of δ_{sw} and vehicle speed V. The map is aligned with the steady-state cornering behaviour of the passive vehicle in high tyre-road friction conditions. To provide safety at different friction levels, a saturation is imposed on the reference yaw rate magnitude, based on the tyre-road friction factor, $\bar{\mu}_f$, at the front axle:

$$|\overline{\dot{\psi}}_{ref,lim}| = \frac{k\bar{\mu}_f g}{V} \tag{1}$$

where k is a constant tuning parameter, and g is the gravitational acceleration. To achieve desirable reference cornering dynamics, the saturated reference signal is sent to a first-order transfer function, which outputs $\overline{\dot{\psi}}_{ref}$.
Here and in the remainder, the notation '$\bar{}$' is used to indicate the vectors with the values of the respective variable, discretised along the prediction horizon t_h. In the case of preview, such variables, along with those dependent on them, change along with the prediction horizon t_h. The analysis of this study, assessing the road preview potential, will not cover the generation method of the preview signals, which will be the object of future research.
(4) The drivability map, computing the total wheel torque demand in traction and braking, $T_{tot,d}$, as a function of p_a, p_b and V.
(5) The online constraint generator, which sets (i) the lower and upper bounds, referred to as $f_{ar,lb/ub}$, on the F2T ARMD ratio, as a function of the current lateral acceleration a_y, to account for the actuation constraints and to prioritise ARMD control when this is effective, i.e. for large $|a_y|$; (ii) the limit, $\alpha_{lim,r}$, on the rear axle slip angle magnitude, which varies linearly with the rear tyre-road friction factor, μ_r, for $0.3 < \mu_r < 0.8$, to become more restrictive in low-friction conditions, and is then saturated to 1.5 deg for $\mu_r \leq 0.3$, and to 4 deg for $\mu_r \geq 0.8$ and (iii) the EM torque limits, $T_{em,lim,ij}$, as a function of the angular wheel speed ω_{ij}, based on the EM characteristic curves.
(6) The NMPC block, providing the individual reference wheel torque levels, T_{ij}, and the reference F2T ARMD ratio, f_{ar}. Only in a specific preview implementation – described later in the text – the controller also outputs the sequence of predicted states and control actions, X and U.

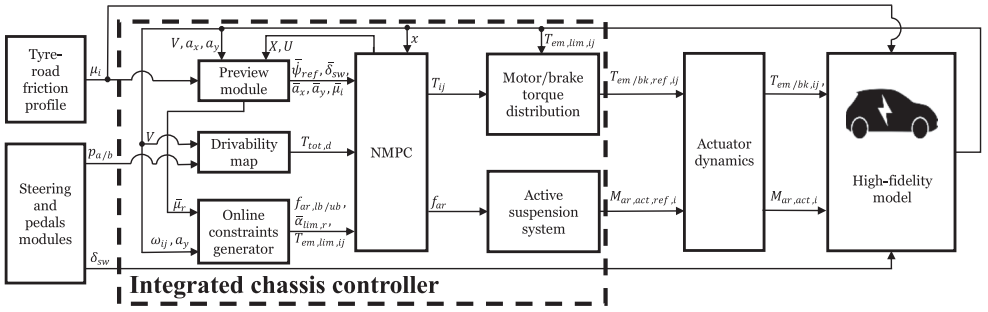

Figure 1. Simplified schematic of the simulation and control framework.

(7) The motor/brake torque distribution block, which, for each corner, splits T_{ij} between the EM, corresponding to the torque contribution $T_{em,ref,ij}$, and the friction brake actuator, corresponding to the $T_{bk,ref,ij}$ contribution. Within the corner, the algorithm prioritises regeneration until the respective EM torque limit is reached.

(8) The ASS block, which computes – from the lateral acceleration – the total reference anti-roll moment for the active suspension actuators, and distributes it among the front and rear axles based on f_{ar}, thus generating the reference anti-roll moments $M_{ar,act,ref,i}$.

(9) The actuator dynamics block, using first-order transfer functions to obtain the actuation outputs – from the EMs, friction brakes and ASS, respectively, $T_{em,ij}$, $T_{bk,ij}$ and $M_{ar,act,i}$ – that are applied to the vehicle.

(10) The high-fidelity vehicle model, which provides the state vector x, along with other measured variables, to the control architecture, and is set up through the Simulink interface of the VSM simulation software package [47] by AVL. The model includes the six degrees of freedom (DoFs) of the sprung mass, and the rotational and vertical DoFs of each unsprung mass. The coupling among the DoFs is considered, together with the suspension compliances. Tyre nonlinearities are accounted for through version 5.2 of the Pacejka magic formula, including relaxation effects [48]. The model was experimentally validated along quasi-steady-state and transient vehicle tests – executed by AVL – on the baseline EV demonstrator without TV nor ASS. For example, Figure 2 reports the results along a 40 m radius skidpad, and a transient steering manoeuvre. The good match between simulations and experiments makes the model a valuable tool for control system assessment.

3. Control strategies

3.1. Prediction model formulations

The prediction – or internal – model is used by the NMPC algorithm to predict the system dynamics along t_h. The model is formulated as follows, see also Figure 3:

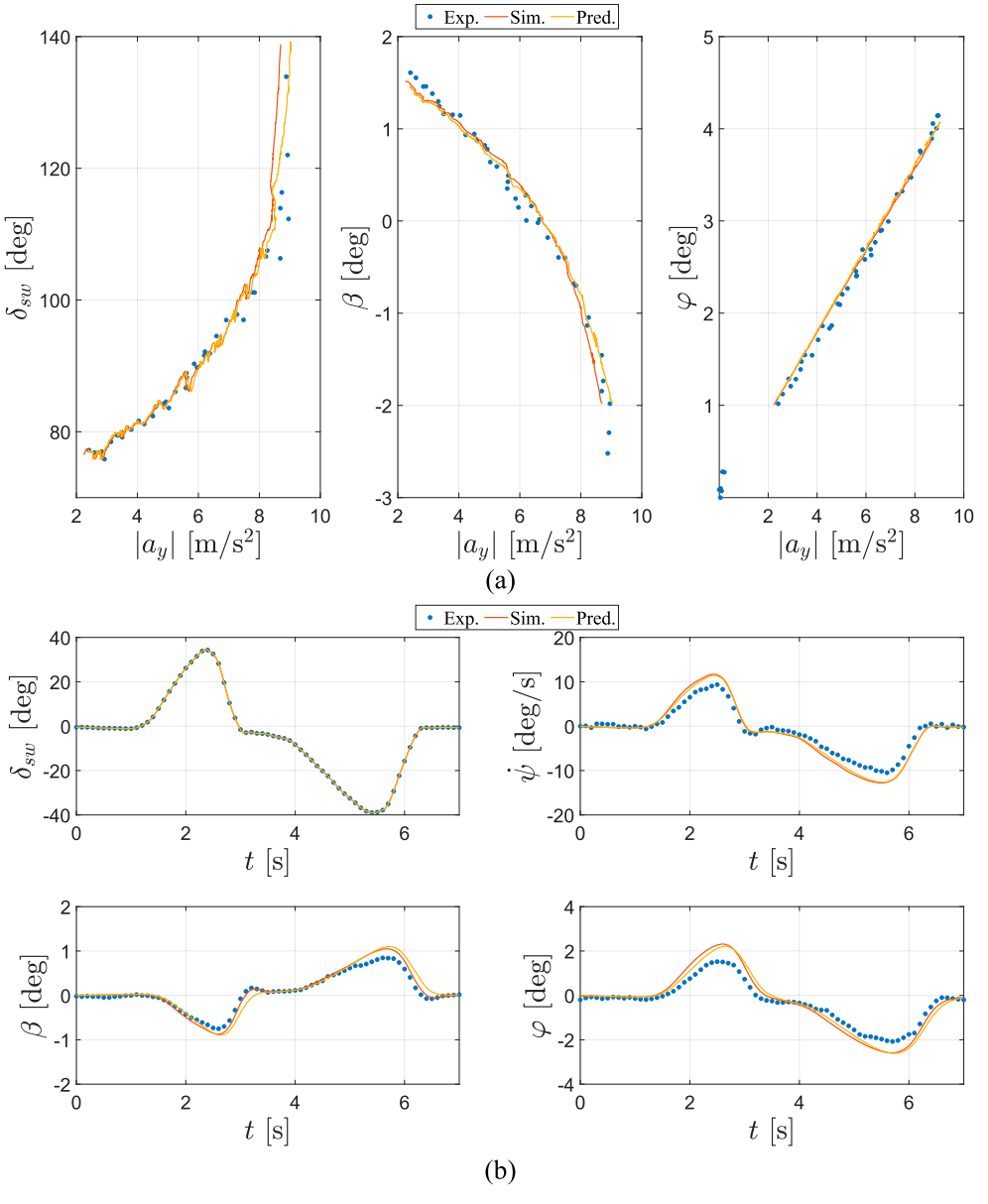

Figure 2. Examples of validation of the NMPC prediction model ('Pred.') and high-fidelity VSM vehicle model ('Sim.') with experimental data ('Exp.') along: (a) a skidpad manoeuvre and (b) a transient steering manoeuvre.

- Force balance along the direction of the velocity vector at the centre of gravity (CG)

$$\dot{V} = \frac{1}{m}\left\{\cos(\beta)\left\{\sum_{i=f,r}\sum_{j=l,r}[F_{x,ij}\cos(\delta_{ij}) - F_{y,ij}\sin(\delta_{ij})] - F_{drag}\right\}\right.$$
$$\left. + \sin(\beta)\sum_{i=f,r}\sum_{j=l,r}[F_{x,ij}\sin(\delta_{ij}) + F_{y,ij}\cos(\delta_{ij})]\right\} \tag{2}$$

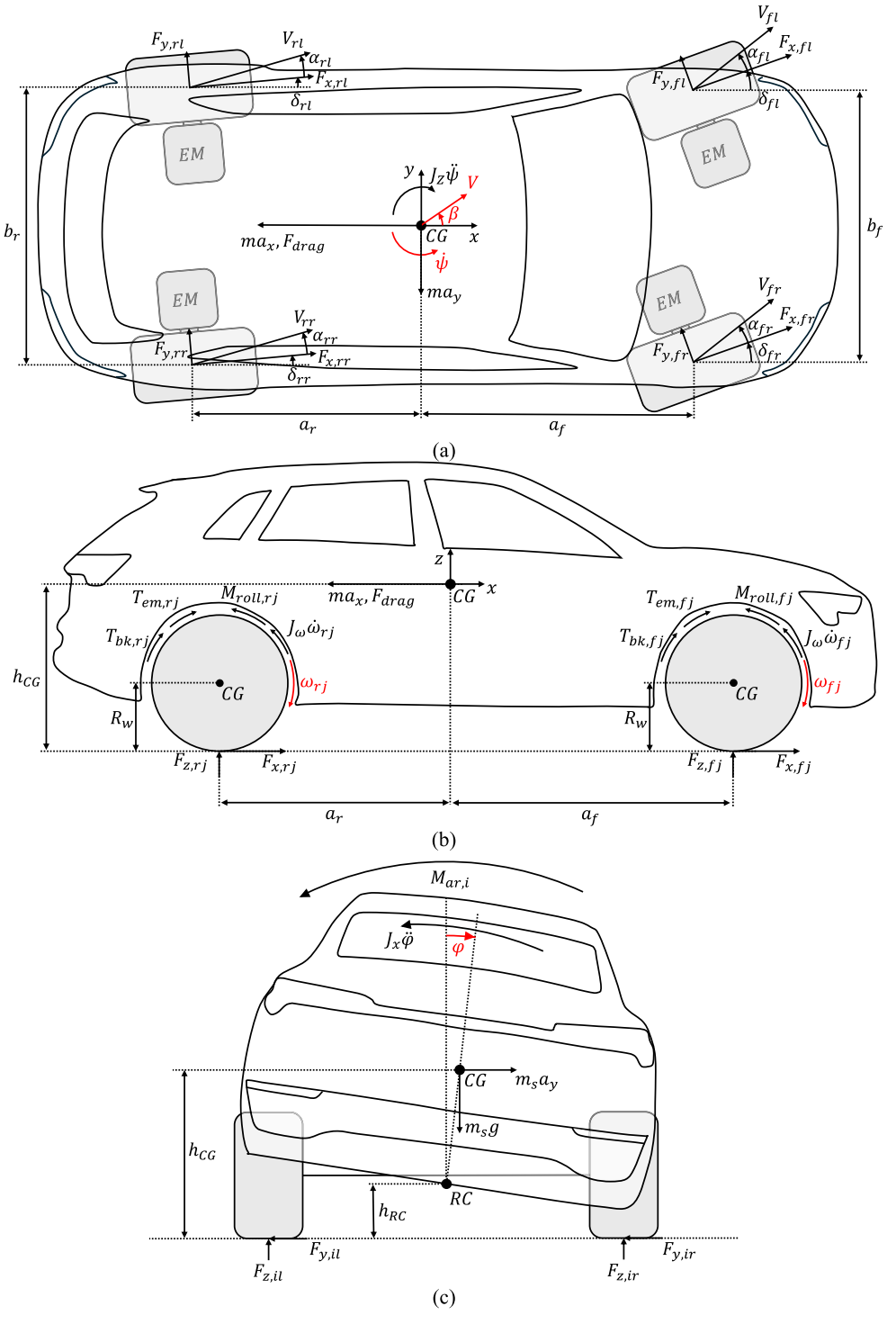

Figure 3. Schematic of the vehicle with the main variables and parameters used within the prediction model: (a) top view; (b) side view and (c) rear view.

where m is the total vehicle mass; β is the sideslip angle; $F_{x,ij}$ and $F_{y,ij}$ are the longitudinal and lateral tyre forces, expressed in the wheel reference frame; δ_{ij} is the steering angle of the wheel ij, whose rear values are kept constant and equal to the static toe contribution $\delta_{s,rj}$; and F_{drag} is the aerodynamic drag force.

- Force balance along the direction perpendicular to the velocity vector at CG

$$\dot{\beta} = \frac{1}{mV}\left\{\cos(\beta)\left\{\sum_{i=f,r}\sum_{j=l,r}[F_{x,ij}\sin(\delta_{ij}) + F_{y,ij}\cos(\delta_{ij})]\right\} - \sin(\beta)\left\{\sum_{i=f,r}\sum_{j=l,r}[F_{x,ij}\cos(\delta_{ij}) - F_{y,ij}\sin(\delta_{ij})] - F_{drag}\right\}\right\} - \dot{\psi} \tag{3}$$

where $\dot{\psi}$ is the yaw rate. Eq. (3) neglects the lateral displacement of the centre of gravity caused by the roll motion, which would bring a marginal accuracy improvement [49] at the price of significantly increasing the computational effort.

- Yaw moment balance

$$\ddot{\psi} = \frac{1}{J_z}\left\{\sum_{j=l,r} a_f[F_{x,fj}\sin(\delta_{fj}) + F_{y,fj}\cos(\delta_{fj})] - \sum_{j=l,r} a_r[F_{x,rj}\sin(\delta_{rj}) + F_{y,rj}\cos(\delta_{rj})] - \sum_{i=f,r}\frac{b_i}{2}[F_{x,il}\cos(\delta_{il}) - F_{y,il}\sin(\delta_{il})] + \sum_{i=f,r}\frac{b_i}{2}[F_{x,ir}\cos(\delta_{ir}) - F_{y,ir}\sin(\delta_{ir})]\right\} \tag{4}$$

where J_z is the yaw mass moment of inertia; a_f and a_r are the front and rear semi-wheelbases and b_f and b_r are the front and rear track widths.

- Roll moment balance

$$\ddot{\varphi} = \frac{1}{J_x}\left\{m_s a_{y,ext}[h_{CG} - h_{RC}]\cos(\varphi) + m_s g[h_{CG} - h_{RC}]\sin(\varphi) - \sum_{i=f,r} M_{ar,i}\right\} \tag{5}$$

where φ is the roll angle; J_x is the roll mass moment of inertia; m_s is the sprung mass; $a_{y,ext}$ is the externally sourced lateral acceleration, which, without preview information, is kept constant along t_h and equal to the measurement from the inertial measurement unit (IMU) or directly coming from the vehicle model when working in a simulation environment; h_{CG} is the CG height from the ground in static conditions; h_{RC} is the roll centre height from the ground; and $M_{ar,i}$ is the total anti-roll moment of each axle, given by the sum of the passive and active contributions:

$$M_{ar,i} = M_{ar,ps,i} + M_{ar,pd,i} + M_{ar,act,i} \tag{6}$$

where $M_{ar,ps,i}$ is the anti-roll moment of the passive springs and anti-roll bars, and $M_{ar,pd,i}$ is the anti-roll moment contribution of the passive dampers.

- Moment balance of the wheel *ij*

$$\dot{\omega}_{ij} = \frac{1}{J_w}[T_{em,ij} + T_{bk,ij} - F_{x,ij}R_w - M_{roll,ij}] \tag{7}$$

where ω_{ij} is the angular wheel speed; J_w is the wheel mass moment of inertia; R_w is the wheel radius; and $M_{roll,ij}$ is the rolling resistance moment.

- Active anti-roll moment dynamics

$$\dot{M}_{ar,act,i} = \frac{M_{ar,act,ref,i} - M_{ar,act,i}}{\tau_{as}} \tag{8}$$

where τ_{as} is the equivalent time constant for ASS actuation; and $M_{ar,act,ref,i}$ is the reference active anti-roll moment for the axle *i*:

$$M_{ar,act,ref,i} = \begin{cases} f_{ar}M_{ar,act,tot}, & i = f \\ [1 - f_{ar}]M_{ar,act,tot}, & i = r \end{cases} \tag{9}$$

- EM torque dynamics

$$\dot{T}_{em,ij} = \frac{T_{em,ref,ij} - T_{em,ij}}{\tau_{em}} \tag{10}$$

where τ_{em} is the EM torque time constant.

- Brake blending approximation

$$T_{em,ref,ij} = \frac{T_{ij} - T_{em,lb,ij}}{1 + e^{-k[T_{ij} - T_{em,lb,ij}]}} + T_{em,lb,ij} \tag{11}$$

where $T_{em,lb,ij}$ is the lower bound of the EM torque, corresponding to maximum braking regeneration capability. Correspondingly, the reference friction braking torque, $T_{bk,ref,ij}$, is computed as

$$T_{bk,ref,ij} = T_{ij} - T_{em,ref,ij} \tag{12}$$

Eqs. (11) and (12) enable a reduction of the number of control inputs of the nonlinear optimal control problem (NOCP), which generates only T_{ij} but is aware of the split between $T_{em,ref,ij}$ and $T_{bk,ref,ij}$.

- Friction brake torque dynamics

$$\dot{T}_{bk,ij} = \frac{T_{bk,ref,ij} - T_{bk,ij}}{\tau_{bk}} \tag{13}$$

where τ_{bk} is the torque time constant of the friction brake actuation.

More detailed descriptions of (2)–(7) and (11), together with the derivations of the slip ratios (σ_{ij}), slip angles (α_{ij}) and vertical tyre loads ($F_{z,ij}$), as well as the adopted simplified (unless otherwise specified) Pacejka tyre model for combined slip conditions, are provided in ref. [5].

Three versions of the prediction model are considered in the following analyses:

- The complete version, including 4 DoFs related to the vehicle body motion (longitudinal, lateral, yaw and roll motions), described by (2)–(5); 4 DoFs related to the wheel

rotations, described by (7); and the ASS, EM and friction brake actuation dynamics, described by (8), (10) and (13).
- An intermediate version, excluding, w.r.t. the complete model, the EM and friction brake dynamics.
- A simplified one, excluding, w.r.t. the intermediate one, the ASS actuation dynamics.

The models are expressed in a nonlinear state-space form, augmented by a state corresponding to the time integral, $\dot{\psi}_{err,int}$, of the error between the reference and actual yaw rate. The corresponding NMPC configurations and variables are referred to with the subscripts 20, 12 and 10, i.e. the number of states of the corresponding internal model, hence the notations NMPC_{20}, NMPC_{12} and NMPC_{10}. Although having formulations that are entirely independent from those of the VSM model for control system assessment, the prediction models are well-aligned, in terms of results, with both the high-fidelity model and experimental data, see Figure 2.

3.2. Nonlinear optimal control problem

The NOCP targets the minimisation of a cost function J, subject to a set of equality and inequality constraints:

$$\underset{U}{\text{argmin}}\ J := J_{terminal} + J_{stage} = \frac{1}{2}\|z_{N_h} - z_{ref,N_h}\|^2_{Q_t} + \frac{1}{2}\sum_{k=0}^{N_h-1}[\|z_k - z_{ref,k}\|^2_Q + \|u_k\|^2_R] \tag{14}$$

s.t.

$$\begin{aligned}
&x_0 = x_{in}\\
&x_{k+1} = f_{pd}(x_k, u_k, p_k)\\
&z_k = g_{pd}(x_k, u_k, p_k)\\
&\text{(i).}\quad T_{tot,lb} \le T_{tot} \le T_{tot,ub}\\
&\text{(ii).}\quad T_{bk,lim,ij} - T_{em,lim,ij} \le T_{ij} \le T_{em,lim,ij}\\
&\text{(iii).}\quad -\sigma_{lim} - z_\sigma \le \sigma_{ij} \le \sigma_{lim} + z_\sigma\\
&\text{(iv).}\quad -\alpha_{lim,i} - z_{\alpha,i} \le \alpha_{ij} \le \alpha_{lim,i} + z_{\alpha,i}\\
&\text{(v).}\quad k_{ebd}[T_{fl} + T_{fr} - \lambda_{bk}T_{tot}] \le 0\\
&\text{(vi).}\quad f_{lb} \le f_{ar} \le f_{ub}\\
&\text{(vii).}\quad -F_{act,lim}b_i \le M_{ar,act,i} \le F_{act,lim}b_i\\
&\text{(viii).}\quad z_\sigma \ge 0\\
&\text{(ix).}\quad z_{\alpha,i} \ge 0
\end{aligned}$$

where J is expressed as the sum of a terminal cost, $J_{terminal}$, referred to the last prediction step, and a stage cost, J_{stage}, computed along t_h; the index k represents a generic time step of t_h; N_h is the number of prediction steps; z_k and z_{N_h} are the predicted system outputs at the steps k and N_h; $z_{ref,k}$ and z_{ref,N_h} are the reference values of the outputs along and at the end of t_h; the vector U includes the optimal control input sequence along t_h, i.e. $U = [u_0, u_1, \ldots, u_k, \ldots, u_{N_h}]$; Q and Q_t are the weight matrices of the stage and terminal costs associated with the outputs; R is the cost function weight matrix related to the control actions; x is the state vector; f_{pd} and g_{pd} are the nonlinear functions generating the system states and outputs; p is the vector of the online data; T_{tot} is the sum of the reference wheel

torque values provided by the NMPC; $T_{tot,lb}$ and $T_{tot,ub}$ are the variable lower and upper boundaries on T_{tot}; $T_{bk,lim,ij}$ is the friction braking torque limit; σ_{lim} is the limit on the longitudinal tyre slip ratio, which is used to implement the traction and anti-lock braking system functionalities; z_σ and $z_{\alpha,i}$ are slack variables, defining soft constraints on the tyre slip ratios σ_{ij} and front and rear slip angles α_{ij}; k_{ebd} is a boolean variable related to the activation of the electronic brake distribution function; λ_{bk} is the limit value of the braking torque distribution factor and $F_{act,lim}$ is the ASS force limit.

The NOCP in (14) embeds constraints (i)–(ix), where (i) limits the total torque range; (ii) sets the torque limit on each corner, which is larger in magnitude in case of a braking request; (iii) and (iv) constrain the tyre slip ratios and front and rear slip angles, where the soft formulation facilitates the solution of the optimisation problem also in the most challenging scenarios [50]; (v) sets the F2T torque distribution range during braking; (vi) imposes the F2T ARMD factor range; (vii) defines the limit on the front and rear suspension anti-roll moments; and (viii) and (ix) define the constraints on the slack variables, which must be non-negative for the respective constraints to be physically meaningful.

The components of x depend on the considered prediction model:

$$\begin{aligned} x_{10} &= [V, \beta, \dot{\psi}, \dot{\varphi}, \varphi, \omega_{fl}, \omega_{fr}, \omega_{rl}, \omega_{rr}, \dot{\psi}_{err,int}] \\ x_{12} &= [V, \beta, \dot{\psi}, \dot{\varphi}, \varphi, \omega_{fl}, \omega_{fr}, \omega_{rl}, \omega_{rr}, \dot{\psi}_{err,int}, M_{ar,act,f}, M_{ar,act,r}] \\ x_{20} &= [V, \beta, \dot{\psi}, \dot{\varphi}, \varphi, \omega_{fl}, \omega_{fr}, \omega_{rl}, \omega_{rr}, \dot{\psi}_{err,int}, M_{ar,act,f}, M_{ar,act,r}, T_{em,fl}, \\ &\quad T_{em,fr}, T_{em,rl}, T_{em,rr}, T_{bk,fl}, T_{bk,fr}, T_{bk,rl}, T_{bk,rr}] \end{aligned} \tag{15}$$

The control input vector is given by:

$$u = [T_{fl}, T_{fr}, T_{rl}, T_{rr}, f_{ar}, z_\sigma, z_{\alpha,f}, z_{\alpha,r}] \tag{16}$$

The NOCP is also characterised by online parameters, which are kept constant along t_h, unless they are externally obtained as road preview information:

$$\begin{aligned} p = [&\delta_{fl}, \delta_{fr}, a_x, a_y, \mu_f, \mu_r, T_{em,lim,fl}, T_{em,lim,fr}, T_{em,lim,rl}, T_{em,lim,rr}, f_{ar,lb}, f_{ar,ub}, \alpha_{r,lim}, \\ &\dot{\psi}_{ref}, T_{tot,ub}, T_{tot,lb}, k_{ebd}] \end{aligned} \tag{17}$$

where, in the most complex configuration, the preview information will be available for δ_{fj}, a_x, a_y, μ_i, $\dot{\psi}_{ref}$ and $\alpha_{r,lim}$.

The terms of J_{stage} account for:

- $\dot{\psi}_{err}$, which is given by the linear combination of the yaw rate error and its time integral:

$$\dot{\psi}_{err} = \dot{\psi} - \dot{\psi}_{ref} + w\dot{\psi}_{err,int} \tag{18}$$

  where w is a constant calibration parameter.
- ΔT_{tot}, which aims to fulfil the driver torque request, computed by the drivability map:

$$\Delta T_{tot} = \sum_{i=f,r} \sum_{j=l,r} T_{ij} - T_{tot,d} \tag{19}$$

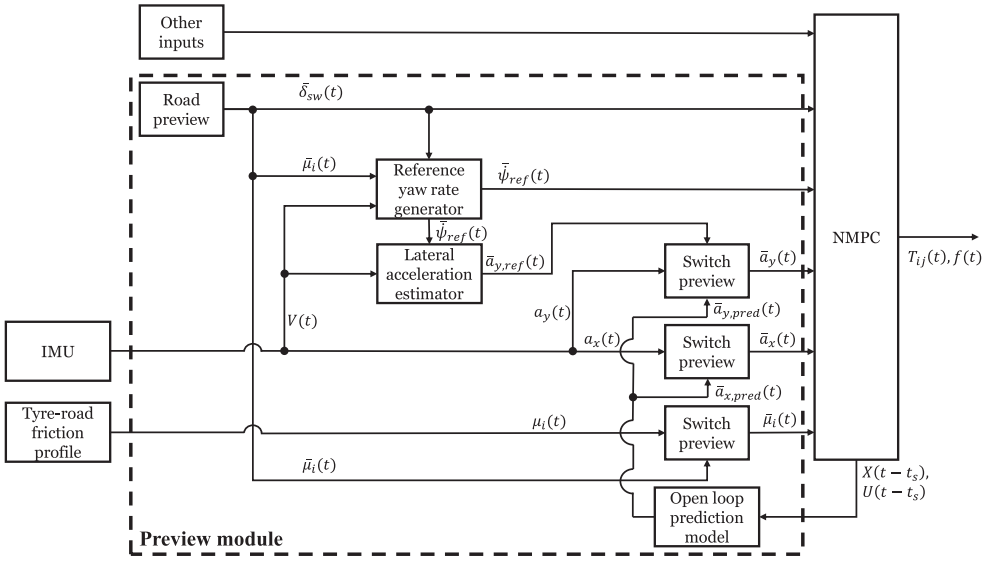

Figure 4. Road preview module schematic.

- Δf_{ar}, which aims to keep ARMD close to the nominal value, $f_{ar,pass}$, of the passive configuration of the same EV:

$$\Delta f_{ar} = |f_{ar} - f_{ar,pass}| \tag{20}$$

- z_σ, $z_{\alpha,f}$ and $z_{\alpha,r}$, which have been introduced in (14).

The terminal cost, $J_{terminal}$, facilitating system stability, only consists of $\dot{\psi}_{err}$.

3.3. Road preview

The road preview concept is summarised in Figure 4. The considered road preview vectors along t_h are:

- $\bar{\delta}_{sw}$, including the sequence of expected steering wheel inputs, which could be obtained through: (i) the V2X communication of the driver profiles of the vehicles ahead or driving behaviour predictors, in the case of human-driven vehicles. For example, in ref. [51], an AI-based approach is proposed to model the human driver behaviour through a recurrent neural network that considers as inputs the historical speeds, historical road curvatures, future road curvatures, and historical steering wheel angles, and provides as outputs the sequence of future steering wheel angles; or (ii) the higher-level path tracking system, in the case of driving automation, since the path tracking layer usually generates a predicted steering angle profile for a longer horizon [33] – generally with a range from 0.5 to 2 s – than the one required for chassis control. The steering angle preview is expected to be particularly significant in manoeuvring conditions with high $|\dot{\delta}_{sw}|$.

- $\bar{\dot{\psi}}_{ref}$, including the sequence of reference yaw rate values, which is computed from $\bar{\delta}_{sw}$, $\bar{\mu}_f$, and V, where the latter is kept constant along t_h.
- $\bar{a}_{y,ref}$, i.e. the sequence of lateral acceleration values, obtained under the quasi-steady-state assumption that along t_h the vehicle tracks the reference yaw rate profile with zero sideslip rate, while remaining at the current V:

$$a_{y,ref} = V\dot{\psi}_{ref} \tag{21}$$

  which enables the prediction of the lateral load transfer profile.
- $\bar{a}_{x,pred}$ and $\bar{a}_{y,pred}$, including the prediction of the longitudinal and lateral acceleration profiles, through the open-loop prediction model implementation. At each time step, the NMPC algorithm generates the sequences, U and X, of the optimal control actions and predicted vehicle states along t_h. While the control actions at the first step are provided as reference values to the ASS, EMs and friction brakes, the information along t_h is used to calculate the accelerations at each time instant, based on the internal model equations. Thus, at a generic time instant t, the predicted acceleration vectors are:

$$\begin{aligned}\bar{a}_{x,pred}(t+t_s) = [&a_{x,pred}(t+t_s|t), a_{x,pred}(t+2t_s|t), \ \ldots, \ a_{x,pred}(t+kt_s|t),\\ &\ldots, a_{x,pred}(t+N_h t_s|t), a_{x,pred}(t+N_h t_s|t)]\\ \bar{a}_{y,pred}(t+t_s) = [&a_{y,pred}(t+t_s|t), a_{y,pred}(t+2t_s|t), \ \ldots, \ a_{y,pred}(t+kt_s|t),\\ &\ldots, a_{y,pred}(t+N_h t_s|t), a_{y,pred}(t+N_h t_s|t)]\end{aligned} \tag{22}$$

  where t_s is the NMPC sampling time; and the last two values of the components of each vector are repeated, because of the lack of prediction information from the previous time step. In the following analyses, $\bar{a}_{y,pred}$ is used as a more advanced alternative to $\bar{a}_{y,ref}$.
- $\bar{\alpha}_{lim,r}$, which sets variable limits on the rear slip angles, depending on $\bar{\mu}_r$, as introduced in Section 2.
- $\bar{\mu}_i$, which may be known in advance through next-generation exteroceptive sensor information processing and V2X communication. While improving prediction accuracy during the NOCP solution, the friction coefficient preview also anticipates the changes of $\dot{\psi}_{ref}$ and $\alpha_{lim,r}$. The front and rear tyre-road friction factors are directly derived from the same tyre-road friction map**.** Given the focus on the assessment of the road preview control benefits rather than the development of preview signal generation functionalities, no tyre-road friction preview generator or estimator has been implemented in this study. Unless otherwise specified, in the remainder, the tyre-road friction information is assumed to be sent without errors or delays to the controllers.

Five NMPC configurations are analysed, based on their road preview typology:

- $\text{NMPC}_{\text{base}}$, which does not include any form of preview, i.e. the online parameters are kept constant along t_h.
- $\text{NMPC}_{\text{prev}}$, which considers the preview only within $\bar{\delta}_{sw}$ and $\bar{\dot{\psi}}_{ref}$.
- $\text{NMPC}_{\text{prev,ay,ref}}$, which, on top of the previews in $\text{NMPC}_{\text{prev}}$, considers a variability within $\bar{a}_y$, whose elements are given by $a_{y,ref}$ in (21).

- $\text{NMPC}_{\text{prev,ay,pred}}$, which, differently from $\text{NMPC}_{\text{prev,ay,ref}}$, uses $\bar{a}_{y,pred}$ as preview information.
- $\text{NMPC}_{\text{prev,}\mu}$, which adds the $\bar{\mu}_i$ and $\bar{a}_{x,pred}$ previews to those of $\text{NMPC}_{\text{prev,ay,pred}}$.

The 'switch preview' blocks in Figure 4 are used to activate or deactivate preview functionalities, depending on the selected configuration, as listed above.

3.4. Controller implementation

The ACADO toolkit [3] was used to compute the implicit (i.e. online) solution of the proposed NMPCs, through iterative Gauss–Newton algorithms. The NOCP is converted into a Quadratic Programming (QP) problem, which is solved by the qpOASES 3 solver. The discretisation time of the internal model is set to 1 ms, while the number of prediction steps N_h and the controller sampling time t_s are varied depending on the presented analysis. Unless otherwise specified, the number N_{iter} of iterations, i.e. the number of times the NOCP is solved at each time step, is equal to 3. A Matlab interface allows exporting, compiling, and using autogenerated C code for NMPCs, also enabling real-time implementation, which – where indicated – was achieved through a dSPACE MicroAutoBox III device.

3.5. Controller calibration

To highlight the potential of the individual controller setups and for the fairness of comparison, the NMPC cost function weights in (14), namely Q, Q_t and R, are optimised for each of the manoeuvres in Section 4, within reasonably broad variation ranges. The optimisation routine uses the 'surrogateopt' tool of Matlab, targeting the global minimisation of the cost function J_{WT}:

$$\underset{Q,Q_t,R}{\text{argmin}}\ J_{WT} = w_{WT1}\frac{\dot{\psi}_{RMSE}}{\max(\dot{\psi}_{RMSE})} + w_{WT2}\frac{\Delta T_{tot,RMS}}{\max(\Delta T_{tot,RMS})} + w_{WT3}\frac{\Delta\alpha_{r,max}}{\max(\Delta\alpha_{r,max})} + w_{WT4}\frac{\Delta\alpha_{r,RMS}}{\max(\Delta\alpha_{r,RMS})}$$

s.t.

$$\begin{aligned} Q, Q_t &\in [Q_{min}, Q_{max}] \\ R &\in [R_{min}, R_{max}] \end{aligned} \tag{23}$$

where the individual cost function terms refer to:

- The root mean square error value, $\dot{\psi}_{RMSE}$, of the actual yaw rate w.r.t. its reference value:

$$\dot{\psi}_{RMSE} = \sqrt{\frac{1}{T_2 - T_1}\int_{T_1}^{T_2}[\dot{\psi} - \dot{\psi}_{ref}]^2 dt} \tag{24}$$

where T_1 and T_2 are the initial and final times of the relevant part of the test.

- The root mean square error value, $\Delta T_{tot,RMS}$, of the magnitude of the total wheel torque reduction w.r.t. the driver torque request:

$$\Delta T_{tot,RMS} = \sqrt{\frac{1}{T_2 - T_1}\int_{T_1}^{T_2}\left[\sum_{i=f,r}\sum_{j=l,r} T_{ij} - T_{tot,d}\right]^2 dt} \tag{25}$$

- The maximum violation, $\Delta\alpha_{r,max}$, of the rear slip angle limit:

$$\Delta\alpha_{r,max} = \max(\Delta\alpha_r) \tag{26}$$

with $\Delta\alpha_r$ being:

$$\Delta\alpha_r = \max\left(0, \left|\frac{\sum_{j=l,r}\alpha_{rj}}{2}\right| - \alpha_{lim,r}\right) \tag{27}$$

- $\Delta\alpha_{r,RMS}$, i.e. the root mean square error value of the violation $\Delta\alpha_r$ of the rear slip angle limit:

$$\Delta\alpha_{r,RMS} = \sqrt{\frac{1}{T_2 - T_1}\int_{T_1}^{T_2}\Delta\alpha_r{}^2 dt} \tag{28}$$

In the tests with variable tyre-road friction conditions, the weights w_{WT} are set to particularly penalise the yaw rate tracking error and slip angle violation, while achieving an acceptable torque demand error. In high tyre-road friction conditions, only the yaw rate tracking term of (23) is used.

4. Simulation results

The following analyses are carried out with the high-fidelity VSM model from Section 2, with the exception of the sensitivity simulations in Figure 7(c), for which the internal NMPC model is used as the plant model. Among the considered configurations, the passive one refers to the vehicle with ASS for roll angle control, but without TV nor ARMD functionality. Unless otherwise specified, all results are obtained after the application of the optimisation routine in Section 3.5 to the specific manoeuvre and controller setting.

4.1. Considered manoeuvres

Three manoeuvres with the same initial conditions, i.e. 100 km/h of vehicle speed with 20% accelerator pedal position, are implemented to compare the preview configurations:

- Manoeuvre 1, i.e. an extreme sinusoidal steering manoeuvre with a steering wheel angle amplitude of 160 deg at a frequency of 0.8 Hz, performed on a high-friction road with constant accelerator pedal input, reaching a maximum lateral acceleration of ~ 1 g.
- Manoeuvre 2, having the same steering angle and accelerator pedal profiles as the first one, but also involving a sequence of positive and negative high-amplitude tyre-road friction factor steps, with $0.3 \leq \mu \leq 1.25$.

- Manoeuvre 3, i.e. a multiple-step steer test with a steering wheel angle magnitude of 80 deg applied at a rate of 400 deg/s, on a road with abrupt high-to-low and low-to-high μ variations, concurrently with step torque demand transitions, i.e. a first one from a positive torque demand to a negative request to reach a deceleration of $\sim$5 m/s^2, and a second one to $p_a = 80\%$, corresponding to an acceleration exceeding 3 m/s^2.

4.2. Effect of the road preview on prediction model fidelity

Figure 5 reports the simulation results for $\text{NMPC}_{\text{base,10}}$ (Figure 5(a)), $\text{NMPC}_{\text{prev,10}}$ (Figure 5(b)), and $\text{NMPC}_{\text{prev,ay,pred,10}}$ (Figure 5(c)), during Manoeuvre 1. For simplicity, in this preliminary analysis, the actuation dynamics are neglected in the prediction and plant models. N_h is set to 7, and t_s varies along the prediction, i.e. the respective vector is $T_s = [25, 25, 25, 25, 50, 50, 100]$ ms, corresponding to $t_h = 300$ ms. The 'Actual' curves are the response profiles of the main vehicle variables from the VSM model, while the 'Prediction' curves are the prediction profiles along t_h, for specific time instants (every 0.6 s for ease of interpretation) during the simulations. Hence, the quality of the prediction can be inferred through the comparison of the 'Actual' and 'Prediction' curves.

$\text{NMPC}_{\text{base,10}}$, which is the benchmarking configuration, does not provide an accurate $\dot{\psi}$ prediction but still guarantees an acceptable β prediction. The steering angle preview of $\text{NMPC}_{\text{prev,10}}$ brings a significant improvement of all predictions, with the exception of φ and a_y, where the latter one – being implemented as a constant online parameter – does not vary along t_h. With the introduction of the $\bar{a}_{y,pred}$ preview, $\text{NMPC}_{\text{prev,ay,pred,10}}$ generates significantly more accurate predictions of φ, a_y, and the lateral load transfers.

For a quantitative assessment, the root mean square error (RMSE) between the predicted and actual responses is used as a key performance indicator (KPI). At each time step – when the NMPC provides the new set of predictions – the RMSE values are computed for the entire prediction vector. The maximum and mean RMSE values over the simulations are used to evaluate the overall performance, see Figure 6. With respect to $\text{NMPC}_{\text{base,10}}$, $\text{NMPC}_{\text{prev,10}}$ brings an average 23% reduction of both the maximum and mean RMSE values across the variables, while $\text{NMPC}_{\text{prev,ay,pred,10}}$ reduces the respective RMSE values by a further 42% and 35% w.r.t. $\text{NMPC}_{\text{prev,10}}$.

4.3. Sensitivity to controller settings and actuation dynamics

The objective is to guide the t_h selection for each NMPC configuration. In Figure 7(a), referring to Manoeuvre 1, $\Delta\dot{\psi}_{RMSE,}$ represents the reduction – expressed in percentage – of $\dot{\psi}_{RMSE}$ for the NMPC algorithms (i.e. $\dot{\psi}_{RMSE,NMPC}$), w.r.t. the corresponding value – referred to as $\dot{\psi}_{RMSE,Pass}$ – for the passive configuration, i.e. $\Delta\dot{\psi}_{RMSE} = 100\{1 - [\dot{\psi}_{RMSE,NMPC}/\dot{\psi}_{RMSE,Pass}]\}$. In the reported results as a function of t_h, the actuator dynamics are neglected both in the high-fidelity simulation model and the prediction model. The sensitivity is performed for two versions of the tyre model included in the internal model: (i) the simplified Pacejka model mentioned in Section 3.1 and (ii) the complete version 5.2 of the Pacejka magic formula, indicated with 'MF52'. In the simulations, the high-fidelity VSM model always uses the advanced tyre model formulation. With respect to the internal model, the VSM model also includes the heave and pitch dynamics of the sprung mass, the vertical dynamics of each unsprung mass, the complete coupling among

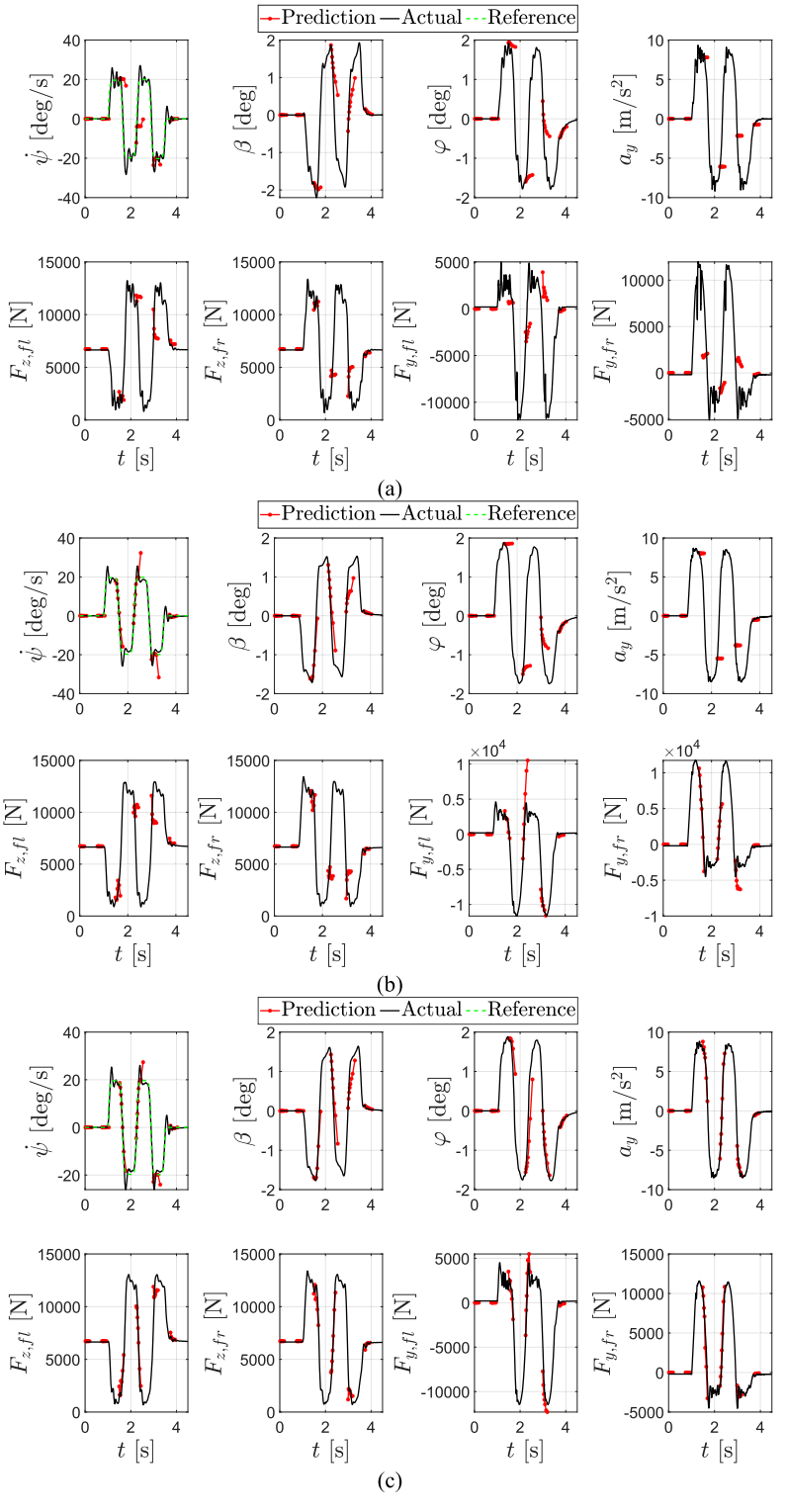

Figure 5. Internal model predictions ('Prediction') and actual profiles ('Actual') of the main vehicle response variables, during Manoeuvre 1 (for the yaw rate, also the reference profile is reported), for: (a) $\text{NMPC}_{\text{base},10}$, (b) $\text{NMPC}_{\text{prev},10}$ and (c) $\text{NMPC}_{\text{prev,ay,pred},10}$.

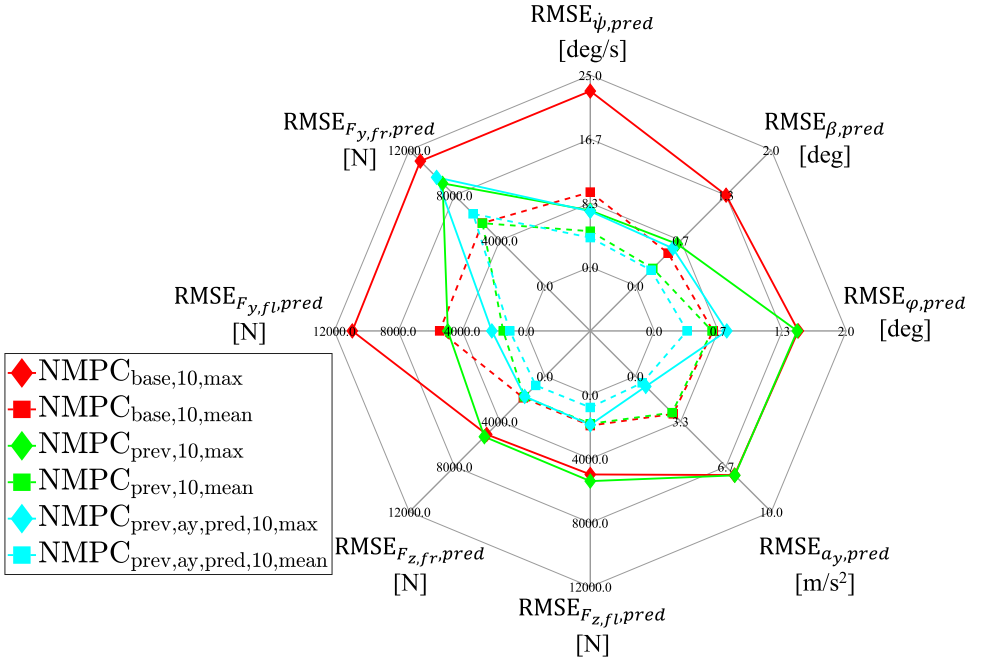

Figure 6. Maximum (corresponding to the subscript 'max' in the legend) and mean (corresponding to the subscript 'mean' in the legend) values of the root mean square errors of the predictions, computed along Manoeuvre 1. The considered variables are indicated in the subscript of each RMSE notation.

the degrees of freedom, and the full suspension kinematic and compliance characteristics. Indeed, the prediction model and VSM model are based on completely independent formulations, which inherently provide a form of controller robustness verification.

In the figure, up to $t_h = 100$ ms, t_s is set to 25 ms; for $t_h = 200$ ms, the additional two steps have $t_s = 50$ ms; finally, for $t_h = 300$ ms, a single 100 ms step is added. NMPC$_{\text{base,10}}$ and NMPC$_{\text{base,MF52,10}}$ provide quite uniform performance as a function of t_h, with $\Delta\dot{\psi}_{RMSE}$ ranging from $\sim$65% to $\sim$72%, and an average $\sim$5% benefit brought by the more advanced tyre model. NMPC$_{\text{prev,10}}$ and NMPC$_{\text{prev,MF52,10}}$, embedding the preview on δ_{sw}, further increase $\Delta\dot{\psi}_{RMSE}$ by almost 20% at $t_h = 75$ ms, which is a major outcome. The best results for the latter configurations are obtained for $t_h = 75$ ms, providing $\sim$7% higher $\Delta\dot{\psi}_{RMSE}$ w.r.t. the cases with $t_h = 200$ and 300 ms. The preview information on the lateral acceleration brings different outcomes depending on the way it is obtained. On the one hand, NMPC$_{\text{prev,ay,ref,10}}$ and NMPC$_{\text{prev,ay,ref,MF52,10}}$ do not manage to reach the performance level of NMPC$_{\text{prev,10}}$ and NMPC$_{\text{prev,MF52,10}}$. On the other hand, across the t_h range, NMPC$_{\text{prev,ay,pred,10}}$ and NMPC$_{\text{prev,ay,pred,MF52,10}}$ bring negligible improvements – amounting to less than 1% – w.r.t. NMPC$_{\text{prev,10}}$ and NMPC$_{\text{prev,MF52,10}}$. Among all configurations, the best results are obtained by NMPC$_{\text{prev,10}}$ and NMPC$_{\text{prev,ay,pred,10}}$ at $t_h = 75$ ms, with $\Delta\dot{\psi}_{RMSE} \approx 87\%$. With the exception of the configurations without preview, i.e. NMPC$_{\text{base,10}}$ and NMPC$_{\text{base,MF52,10}}$, the adoption of the magic formula 5.2 in the prediction model does not bring significant advantages.

Since the computational effort is a key factor in NMPC implementations, the performance assessments in Figure 7(a) are complemented by the analysis of the nondimensional

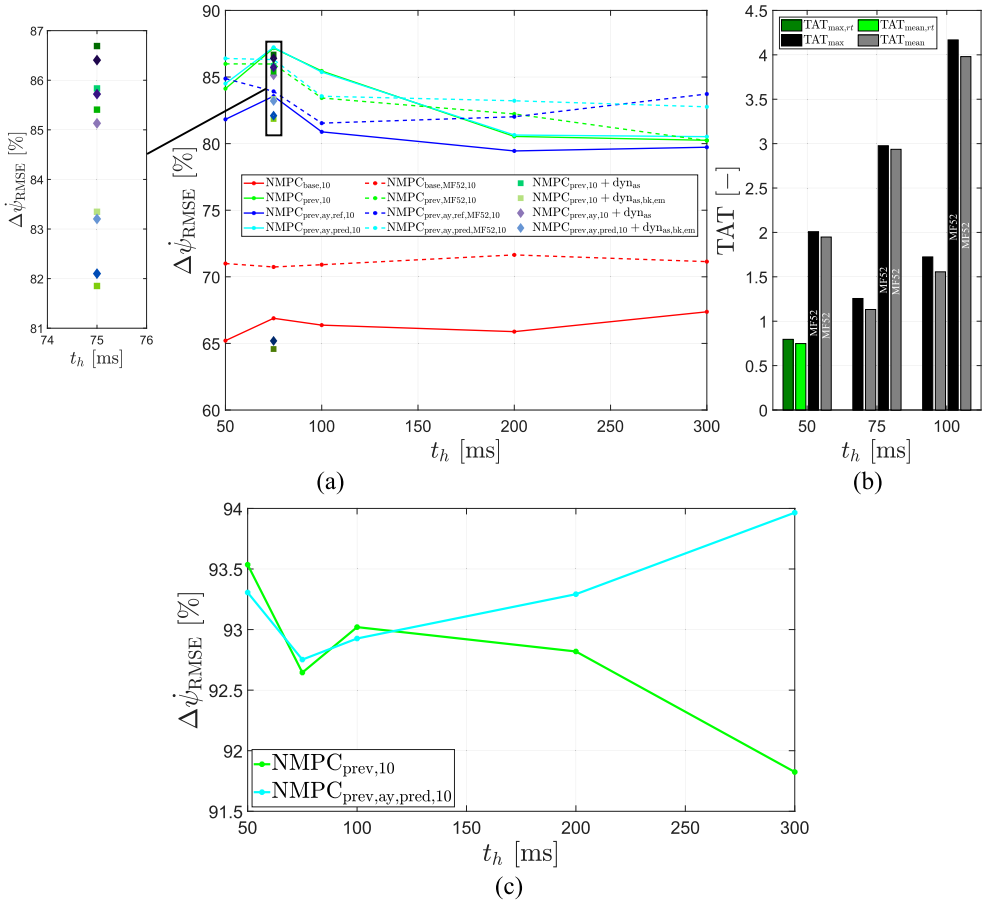

Figure 7. Sensitivity analyses w.r.t. t_h, along Manoeuvre 1: (a) $\Delta\dot{\psi}_{RMSE}$ as a function of t_h for the considered controller configurations, when using the high-fidelity VSM model as plant, (b) Maximum and mean TAT values for NMPC$_{\mathrm{prev,ay,pred,10}}$ and NMPC$_{\mathrm{prev,ay,pred,MF52,10}}$, for $t_h = 50$, 75, and 100 ms and (c) $\dot{\psi}_{RMSE}$ as a function of t_h for NMPC$_{\mathrm{prev,10}}$ and NMPC$_{\mathrm{prev,ay,pred,10}}$, when using the prediction model as the plant model.

turnaround time (TAT), see Figure 7(b), carried out through a dSPACE MicroAutoBox III unit, see also Section 3.4. TAT is the time required for the NMPC to compute the control action, normalised by the sampling time t_s. This means that TAT must be less than 1 for the controller to be real-time implementable on the specific device. Figure 7(b) reports the maximum and mean TAT values, computed for NMPC$_{\mathrm{prev,ay,pred,10}}$ during the relevant part of the simulation. The only real-time implementable case on the selected unit is the one with $t_h = 50$ ms and the simplified tyre model. By including the MF52 model, TAT doubles, while it varies linearly as a function of N_h. Based on the performance and computational analyses of Figures 7(a) and (b), in the remainder, only the NMPC configurations using the simplified tyre model for their predictions are considered.

To analyse the effect of model mismatches, in Figure 7(c), the high-fidelity plant model is replaced with the NMPC prediction model. In this case, the mismatch between the prediction and plant models is obviously lower, and it is caused by the use of online parameters in the NMPC configurations, e.g. constant rather than variable lateral acceleration and thus

lateral load transfer profiles along the prediction horizon, which may lead to degraded performance. This explains why the controller without lateral acceleration preview provides worse performance w.r.t. the one incorporating it. From subplot (a) – (c), the best t_h value for $\text{NMPC}_{\text{prev,ay,pred,10}}$ increases from 75 ms – 300 ms, i.e. the t_h selection strongly depends on the level of internal model mismatch. Instead, the trend for $\text{NMPC}_{\text{prev,10}}$ is the same in subplots (a) and (c). In fact, the lateral acceleration, which is kept constant along t_h, brings significant prediction inaccuracy, and thus worsens controller performance for long t_h. Such interesting results may lead to future studies on neural network model predictive control, where an accurate neural network internal model replaces the simplified physics-based prediction model to enhance prediction quality.

For completeness, for $\text{NMPC}_{\text{prev,10}}$ and $\text{NMPC}_{\text{prev,ay,pred,10}}$ operating at $t_h = 75$ ms, without any cost function weight re-optimisation, Figure 7(a) also reports the $\Delta\dot{\psi}_{RMSE}$ values (see the zoomed inset), resulting from the performance degradation caused by the actuator dynamics, which are only included in the high-fidelity vehicle model. In particular, the notation 'dyn_{as}' refers to the cases with ASS dynamics only, with $\tau_{as} = 40$, 80 and 120 ms, while '$\text{dyn}_{\text{as,bk,em}}$' refers to the cases including the ASS, EM and friction brakes dynamics, with $\tau_{as} = 50$ ms, $\tau_{bk} = 30$ ms and $\tau_{em} = 20$, 50 and 100 ms. The multiplicity of cases corresponds to the cloud of points in the plot. By increasing τ_{as} up to 120 ms, $\Delta\dot{\psi}_{RMSE}$ decreases by $\sim 2\%$. Such negligible variation means that the performance benefit brought by the controller remains approximately constant w.r.t. the passive configuration. However, the active suspension actuation dynamics bring a significant decay of the absolute performance. In fact, for the passive EV, $\dot{\psi}_{RMSE}$ amounts to 11.88, 13.11, 14.61 and 15.93 deg/s for the configurations without ASS actuation dynamics and the three increasing τ_{as} values, which are reflected in the corresponding values for the controlled cases, i.e. 1.52, 1.95, 2.09 and 2.17 deg/s for $\text{NMPC}_{\text{prev,ay,10}}$.

The sensitivity trends w.r.t. t_h do not change by implementing the actuation dynamics in both the high-fidelity and prediction models, as shown in Figure 8. For example, regardless of τ_{as}, $\text{NMPC}_{\text{prev,12}}$ and $\text{NMPC}_{\text{prev,ay,pred,12}}$ provide their best performance for $t_h = 75$ ms, which is selected as the prediction horizon for all the following analyses. Finally, the actuation dynamics – when accounted for in the prediction model formulation – do not significantly influence the control system performance. In fact, in this case, the controlled vehicles experience a very limited 2% $\dot{\psi}_{\text{RMSE}}$ increase w.r.t. the absence of actuation delay. Instead, the corresponding passive vehicle performance decay amounts to 34% for the considered τ_{as} range, since this has an impact on the generation dynamics of the front and rear anti-roll moments, which are still present in the passive case, although their reference distribution among the axles is constant. As a consequence, the $\dot{\psi}_{RMSE}$ improvement relative to the passive vehicle increases from 87.2% in the case of ideal actuation dynamics – see Figure 7(a) – to 90.3% for the highest τ_{as} value. This highlights the effectiveness of the proposed preview architecture also for high values of actuation delay.

Further results related to the actuation dynamics are reported in Figure 9. In particular, in Figure 9(a), only the ASS dynamics are considered in the prediction and high-fidelity plant models, while in Figure 9(b), focusing on the performance effect of τ_{em}, also τ_{as} and τ_{bk}, set to 50 and 30 ms, are included in both models. The two subplots report the $\Delta\dot{\psi}_{RMSE}$ values computed w.r.t. the corresponding NMPC configuration without actuation dynamics in the prediction model, i.e. NMPC_{10}, which is run on the plant model considering the same actuation dynamics as the NMPC for which $\Delta\dot{\psi}_{RMSE}$ is considered. Hence, for

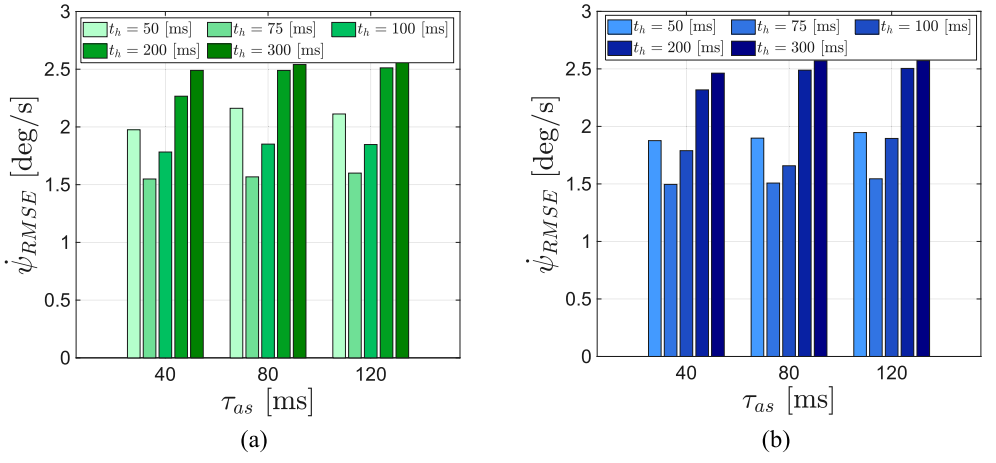

Figure 8. Sensitivity analysis on the prediction horizon t_h for different values of the active suspension force time constant, τ_{as}, for: (a) $\text{NMPC}_{\text{prev},12}$ and (b) $\text{NMPC}_{\text{prev,ay,pred},12}$.

$\text{NMPC}_{\text{base},12}$ and $\text{NMPC}_{\text{base},20}$, $\Delta\dot{\psi}_{RMSE}$ is obtained w.r.t. $\text{NMPC}_{\text{base},10}$, for $\text{NMPC}_{\text{prev},12}$ and $\text{NMPC}_{\text{prev},20}$, w.r.t. $\text{NMPC}_{\text{prev},10}$, and for $\text{NMPC}_{\text{prev,ay,pred},12}$ and $\text{NMPC}_{\text{prev,ay,pred},20}$, w.r.t. $\text{NMPC}_{\text{prev,ay,pred},10}$. If only τ_{as} is considered, the preview configuration achieves $\sim$15–20% improvement. When including the EM dynamics along with the ASS and friction brakes dynamics, the preview improves performance from $\sim$15% to $\sim$60% for $\text{NMPC}_{\text{prev},20}$, and from $\sim$35% to $\sim$60% for $\text{NMPC}_{\text{prev,ay,pred},20}$. Interestingly, without preview, $\text{NMPC}_{\text{base},12}$ and $\text{NMPC}_{\text{base},20}$ do not bring significant improvements w.r.t. $\text{NMPC}_{\text{base},10}$ and can also marginally worsen the results. Table 2 reports the $\dot{\psi}_{RMSE}$ values for the configurations in Figure 9. In the presence of ASS dynamics only, see the first section of the table, the preview configurations provide similar performance among each other, and – importantly – achieve $\dot{\psi}_{RMSE}$ reductions consistently exceeding 50%, w.r.t. the $\text{NMPC}_{\text{base}}$ configurations. With the addition of the EM and friction brakes dynamics, especially for highly responsive IWMs, i.e. with $\tau_{em} \leq 50$ ms, $\text{NMPC}_{\text{prev},20}$ brings an average 71% improvement w.r.t. $\text{NMPC}_{\text{base},20}$, while $\text{NMPC}_{\text{prev,ay,pred},20}$ further reduces $\dot{\psi}_{RMSE}$ by 11%. However, the inclusion of the actuation dynamics in the NMPC internal model increases the computational effort, see Figure 9(c), where, for conciseness, the notations $\text{NMPC}_{10/12/20}$ refer to $\text{NMPC}_{\text{prev,ay,pred},10/12/20}$ in Figure 7(a), for $t_h = 75$ ms. TAT increases approximately linearly with the number of differential equations, i.e. for $\text{NMPC}_{\text{prev,ay,pred},12}$ TAT increases by $\sim$0.3, while for $\text{NMPC}_{\text{prev,ay,pred},20}$ TAT further increases by $\sim$1.9.

Based on the previous results, in the remainder, only the configurations embedding the complete actuation dynamics in the prediction model will be considered, with the time constant values of the nominal plant in Table 1.

Figure 10 reports the sensitivity analysis results on N_{iter}. In the case of a perfect match between prediction and plant models and ideal solver behaviour, the performance should increase with the number of iterations. However, in reality, the optimal N_{iter} is not the largest one. $\text{NMPC}_{\text{base},20}$ obtains an improvement of almost 25% with $N_{iter} = 2$ w.r.t. $N_{iter} = 1$, while the preview configurations, i.e. $\text{NMPC}_{\text{prev},20}$ and $\text{NMPC}_{\text{prev,ay,pred},20}$,

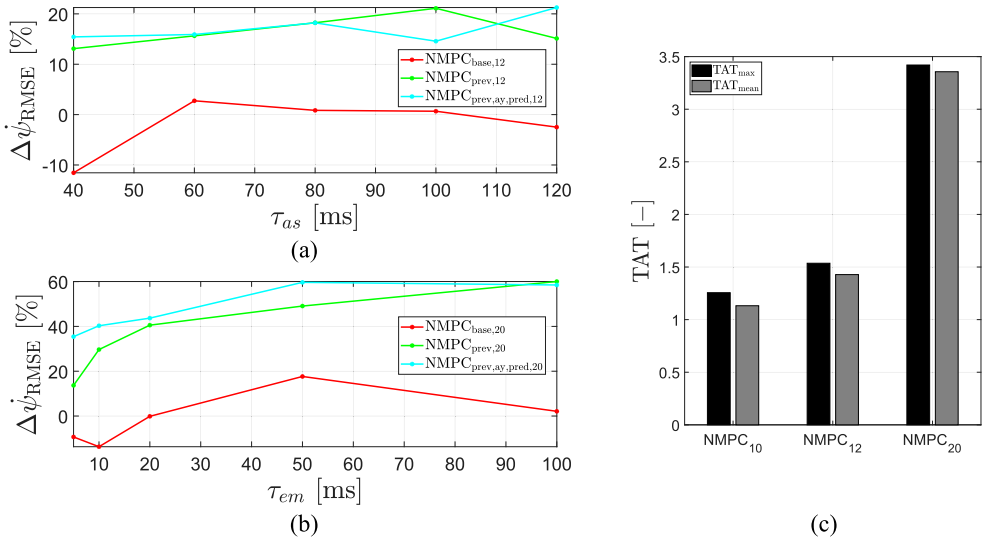

Figure 9. Sensitivity analyses w.r.t. τ_{as} and τ_{em}, along Manoeuvre 1 simulated with the high-fidelity VSM model: (a) $\Delta\dot{\psi}_{RMSE}$ as a function of τ_{as}, (b) $\Delta\dot{\psi}_{RMSE}$ as a function of τ_{em} and (c) Maximum and mean TAT values for NMPC$_{\mathrm{prev,ay,pred,10}}$, NMPC$_{\mathrm{prev,ay,pred,12}}$, and NMPC$_{\mathrm{prev,ay,pred,20}}$, indicated as NMPC$_{10/12/20}$ for ease of notation, computed for the actuation dynamics setup in Table 1.

Table 2. $\dot{\psi}_{RMSE}$ in the presence of actuation dynamics.

$\dot{\psi}_{RMSE}$ [deg/s] with active suspension dynamics only					
Configuration	$\tau_{as} = 40$ ms	$\tau_{as} = 60$ ms	$\tau_{as} = 80$ ms	$\tau_{as} = 100$ ms	$\tau_{as} = 120$ ms
Passive	$1.31{\cdot}10^{1}$	$1.39{\cdot}10^{1}$	$1.46{\cdot}10^{1}$	$1.53{\cdot}10^{1}$	$1.59{\cdot}10^{1}$
NMPC$_{\mathrm{base,10}}$	3.67	3.96	3.95	3.94	3.98
NMPC$_{\mathrm{prev,10}}$	1.78	1.86	1.92	1.90	1.89
NMPC$_{\mathrm{prev,ay,pred,10}}$	1.77	1.82	1.84	1.80	1.96
NMPC$_{\mathrm{base,12}}$	4.09	3.85	3.92	3.92	4.08
NMPC$_{\mathrm{prev,12}}$	1.55	1.57	1.57	1.50	1.60
NMPC$_{\mathrm{prev,ay,pred,12}}$	1.50	1.53	1.51	1.54	1.55
$\dot{\psi}_{RMSE}$ [deg/s] with all actuators dynamics ($\tau_{as} = 50$ ms; $\tau_{bk} = 30$ ms)					
Configuration	$\tau_{em} = 5$ ms	$\tau_{em} = 10$ ms	$\tau_{em} = 20$ ms	$\tau_{em} = 50$ ms	$\tau_{em} = 100$ ms
Passive	$1.35{\cdot}10^{1}$	$1.35{\cdot}10^{1}$	$1.35{\cdot}10^{1}$	$1.35{\cdot}10^{1}$	$1.35{\cdot}10^{1}$
NMPC$_{\mathrm{base,10}}$	4.37	4.29	4.52	5.52	5.31
NMPC$_{\mathrm{prev,10}}$	1.75	1.86	2.10	2.74	3.79
NMPC$_{\mathrm{prev,ay,pred,10}}$	1.94	2.00	2.06	3.20	3.86
NMPC$_{\mathrm{base,20}}$	4.78	4.87	4.52	4.55	5.20
NMPC$_{\mathrm{prev,20}}$	1.51	1.31	1.25	1.39	1.51
NMPC$_{\mathrm{prev,ay,pred,20}}$	1.25	1.19	1.16	1.29	1.60

achieve a 50% $\dot{\psi}_{RMSE}$ reduction if N_{iter} is increased from 1 to 2. Similar to the previous analyses, TAT varies linearly with N_{iter}, but much more significantly, reaching values up to 12 for $N_{iter} = 10$. The results do not significantly vary for $N_{iter} \geq 2$. $N_{iter} = 3$ represents the best selection for NMPC$_{\mathrm{prev,ay,pred,20}}$, and is adopted for all the following analyses.

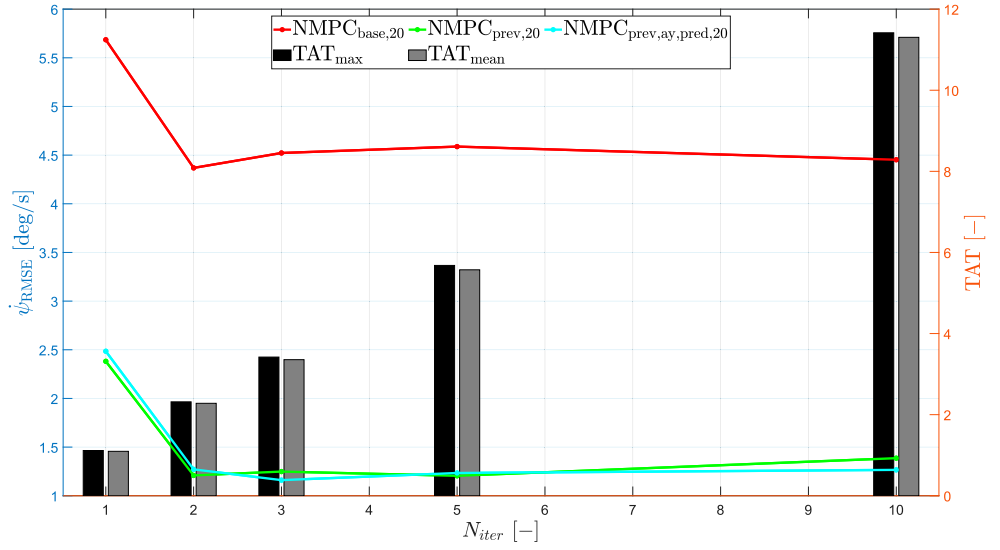

Figure 10. Sensitivity analysis on the number of solver iterations.

4.4. Preview performance in variable friction conditions

Figure 11 reports the time profiles of the main variables along Manoeuvre 2, while Table 3 includes the corresponding KPIs. The plots show the reference yaw rate and the soft constraint thresholds on the average rear slip angle, which vary with the tyre-road friction level. The NMPC$_{\text{prev,}\mu\text{,20}}$ configuration, including the friction factor preview, is introduced, see Section 3.3. Since the NMPCs without μ preview from the previous analyses assume to know the exact tyre-road friction level at each time instant, a more realistic version, NMPC$_{\text{prev,ay,pred,20,est}}$, is added here, with a simulated friction estimation delay. The μ estimation dynamics are approximated through a 25 ms pure time delay, and a first-order transfer function with a 100 ms time constant. On top of being reflected in the predicted vehicle dynamics, the μ delay has an impact on $\dot{\psi}_{ref}$ and $\alpha_{r,max}$, which are used by the NMPC algorithm. Nevertheless, for the fairness of comparison, also for this configuration, the KPIs are computed w.r.t. the ideal reference and constraint.

The passive vehicle generates yaw rate and rear slip angle peaks of −50 deg/s and 14 deg. Without preview, NMPC$_{\text{base,20}}$ reduces $\dot{\psi}_{RMSE}$ by almost 70% w.r.t. the passive configuration, while limiting $\Delta\alpha_{r,max}$. With respect to NMPC$_{\text{base,20}}$, the preview-based configurations NMPC$_{\text{prev,20}}$, NMPC$_{\text{prev,ay,pred,20}}$ and NMPC$_{\text{prev,ay,pred,20,est}}$ decrease $\dot{\psi}_{RMSE}$ by 25%, 26% and 15%, and $\Delta\alpha_{r,max}$ by 36%, 10% and 27%. Interestingly, despite the a_y preview having shown its benefit in Section 4.3, in the presence of highly variable μ, it does not bring any improvement w.r.t. NMPC$_{\text{prev,20}}$. Secondly, with the μ estimation delay, NMPC$_{\text{prev,ay,pred,20,est}}$ provides worse yaw rate tracking than NMPC$_{\text{prev,ay,pred,20}}$, but still better than that of NMPC$_{\text{base,20}}$, with ideal μ information. Thanks to the μ preview, NMPC$_{\text{prev,}\mu\text{,20}}$ improves (respectively by 16% and 7% w.r.t. NMPC$_{\text{prev,20}}$) both KPIs, see also the zoomed plots in Figure 11(b).

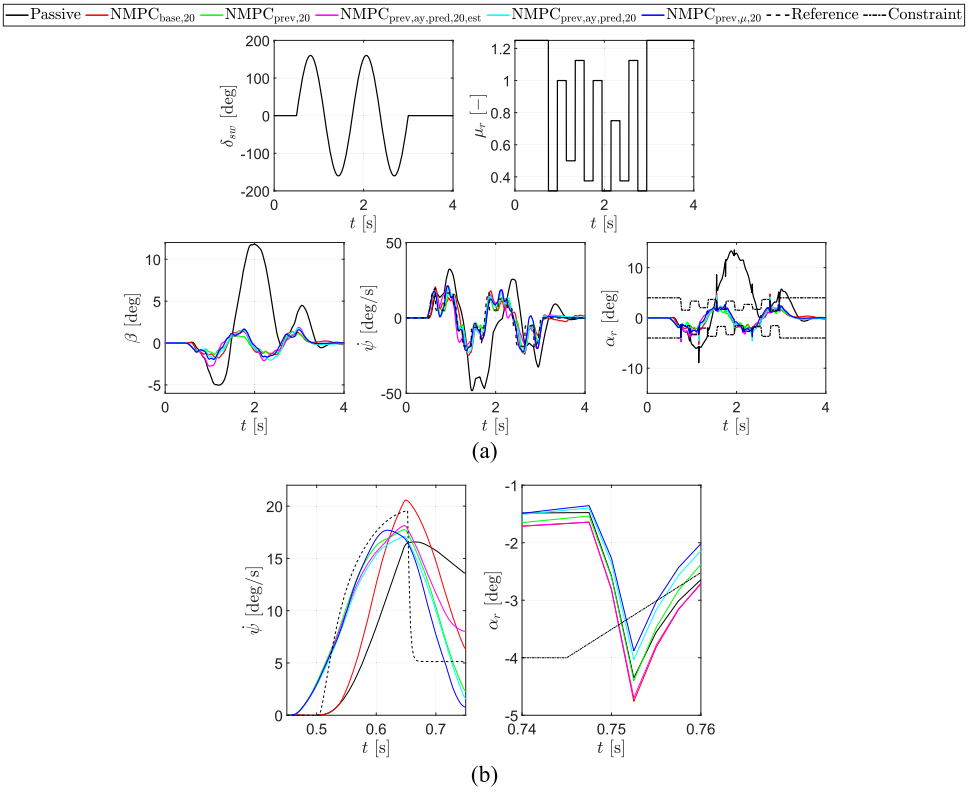

Figure 11. Comparison of the considered NMPC configurations during Manoeuvre 2: (a) time profiles along the whole manoeuvre and (b) zoomed views of specific sections of the test.

Table 3. KPIs for the considered controller configurations along Manoeuvre 2 and Manoeuvre 3.

Configuration	$\dot{\psi}_{RMSE}$ [deg/s]	$\Delta T_{tot,RMS}$ [Nm]	$\Delta\alpha_{r,max}$ [deg]	$\Delta\alpha_{r,RMS}$ [deg]
Manoeuvre 2 – Sinusoidal steering manoeuvre with variable road friction coefficient				
Passive	$1.95{\cdot}10^{1}$	–	$1.13{\cdot}10^{1}$	4.25
NMPC$_{base,20}$	6.11	$6.77{\cdot}10^{2}$	3.08	$2.37{\cdot}10^{-1}$
NMPC$_{prev,20}$	4.59	$6.67{\cdot}10^{2}$	1.96	$9.39{\cdot}10^{-2}$
NMPC$_{prev,ay,pred,20,est}$	5.21	$7.28{\cdot}10^{2}$	2.26	$3.29{\cdot}10^{-1}$
NMPC$_{prev,ay,pred,20}$	4.54	$8.39{\cdot}10^{2}$	2.77	$2.82{\cdot}10^{-1}$
NMPC$_{prev,\mu,20}$	3.86	$1.02{\cdot}10^{3}$	1.83	$2.05{\cdot}10^{-1}$
Manoeuvre 3 – Multiple-step steering manoeuvre with emergency braking and re-acceleration				
Passive	9.91	–	$1.17{\cdot}10^{1}$	7.07
NMPC$_{base,20}$	3.34	$1.65{\cdot}10^{3}$	3.17	$9.63{\cdot}10^{-1}$
NMPC$_{prev,20}$	2.71	$1.69{\cdot}10^{3}$	2.65	$6.51{\cdot}10^{-1}$
NMPC$_{prev,ay,pred,20}$	2.34	$1.64{\cdot}10^{3}$	2.80	$7.84{\cdot}10^{-1}$
NMPC$_{prev,\mu,20}$	2.49	$1.74{\cdot}10^{3}$	1.86	$8.97{\cdot}10^{-1}$

Figure 12 and Table 3 show the Manoeuvre 3 results. With respect to the passive case, NMPC$_{base,20}$ reduces $\dot{\psi}_{RMSE}$ and $\Delta\alpha_{r,max}$ by 66% and 73%. Each preview configuration

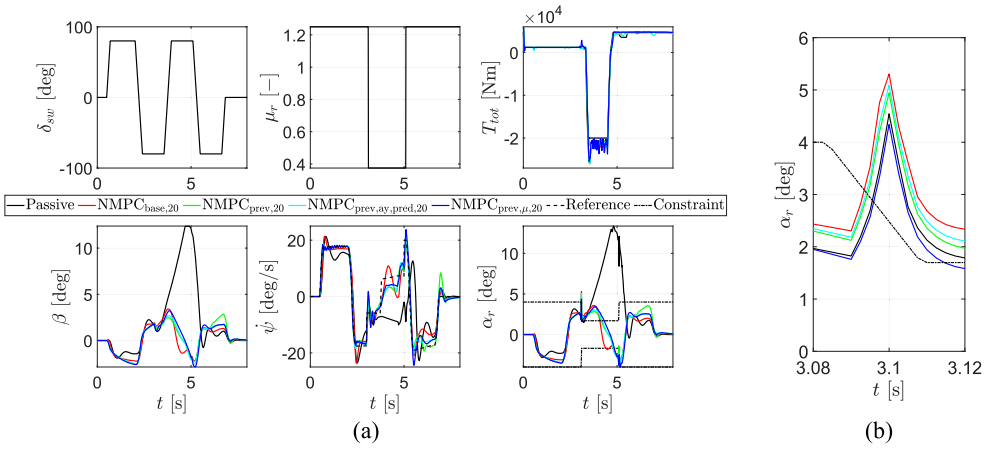

Figure 12. Comparison among the NMPC configurations during Manoeuvre 3: (a) time profiles along the whole manoeuvre; and (b) zoomed view of a specific section of the test.

brings noticeable improvements w.r.t. NMPC$_{base,20}$, with $\dot{\psi}_{RMSE}$ and $\Delta\alpha_{r,max}$ reductions amounting to 19% and 16% for NMPC$_{prev,20}$, 30% and 12% for NMPC$_{prev,ay,pred,20}$, and 25% and 41% for NMPC$_{prev,\mu,20}$.

4.5. Robustness to preview information inaccuracies

Whatever preview technology is going to be adopted for practical implementation, the related information is inevitably affected by inaccuracies. To analyse the robustness of the control architecture with the complete set of preview information, NMPC$_{prev,\mu,20}$ is evaluated in the presence of the following inaccuracies:

- In the NMPC preview vector, the steering wheel input δ_{sw} is replaced by $\delta_{sw,err}$, given by:

$$\delta_{sw,err}(k) = \left[1 + \epsilon_{sw}\frac{k}{N_h}\right]\delta_{sw}(k) \tag{29}$$

  where the preview error magnitude increases along t_h according to k and reaches its maximum value, i.e. ϵ_{sw}, in the last prediction step.
- The tyre-road friction factor preview vector is delayed or anticipated w.r.t. the friction profile $\mu_i(t)$ sent to the VSM model, according to the time shift $t_{\mu,err}$:

$$\bar{\mu}_{i,err,0}(t) = \bar{\mu}_i(t + t_{\mu,err}) \tag{30}$$

  Moreover, the individual shifted elements of $\bar{\mu}_{i,err,0}(t)$ are filtered through first order dynamics with a time constant $\tau_{\mu,err}$:

$$\mu_{i,err,0}(k,t) = \tau_{\mu,err}\dot{\mu}_{i,err}(k,t) + \mu_{i,err}(k,t) \tag{31}$$

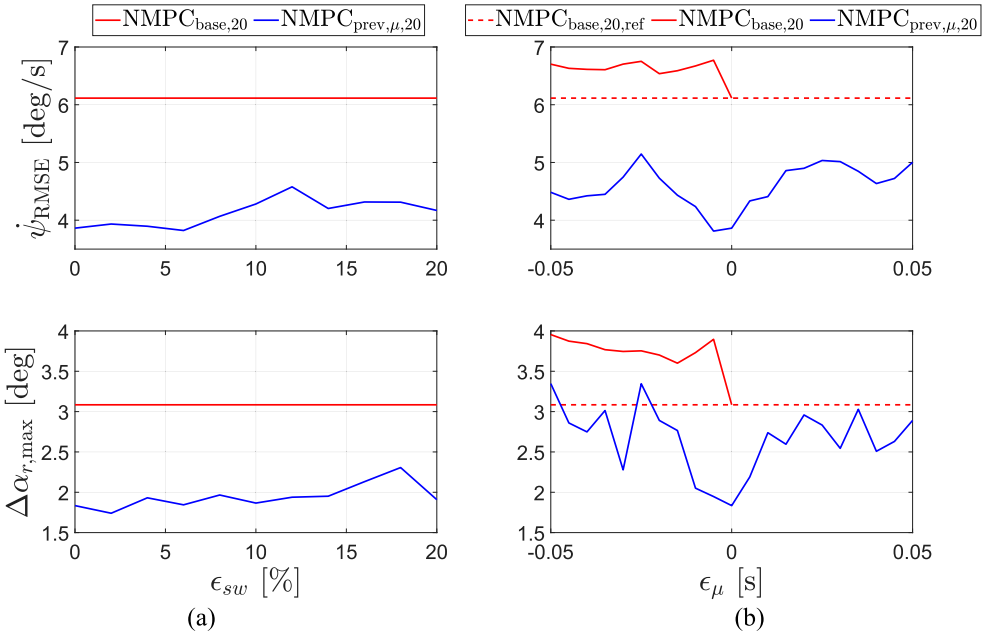

Figure 13. Robustness analysis of NMPC$_{prev,\mu,20}$ w.r.t. (a) the steering wheel angle error parameter ϵ_{sw} and (b) the tyre-road friction factor error parameter ϵ_{μ}, along with Manoeuvre 2, including comparisons with NMPC$_{base,20}$ and NMPC$_{base,20,ref}$.

to obtain the $\mu_{i,err}(k,t)$ profile that is provided to the NMPC algorithm. $\tau_{\mu,err}$ and $t_{\mu,err}$ depend on the parameter ϵ_{μ}:

$$\begin{aligned} \tau_{\mu,err} &= |\epsilon_{\mu}| \\ t_{\mu,err} &= \epsilon_{\mu}/5 \end{aligned} \tag{32}$$

The preview errors on δ_{sw} and μ_i resulting from (29)–(32) propagate on the preview profiles of (i) a_x and a_y, since these are generated through the open-loop integration of the prediction model, see Section 3.3; and (ii) $\dot{\psi}_{ref}$ and $\alpha_{lim,r}$, which directly depend on δ_{sw} and μ_i.

Figure 13 reports the robustness analysis results along Manoeuvre 2, where the KPIs are computed w.r.t. the $\dot{\psi}_{ref}$ and $\alpha_{lim,r}$ profiles in the absence of preview errors. Subplot (a) refers to the sensitivity on ϵ_{sw}, while subplot (b) is on the one on ϵ_{μ}. In addition to NMPC$_{prev,\mu,20}$, the KPIs are included for NMPC$_{base,20}$, i.e. the configuration without preview, which is affected by the error on the current friction coefficient in subplot (b). Hence, subplot (b) also includes NMPC$_{base,20,ref}$, i.e. the configuration without preview that remains unaffected by any friction estimation error. Since in NMPC$_{base,20}$ $\mu_{i,err}$ is supposed to come from an estimator, which is expected to cause lag but not lead shifts. For this configuration, the results are reported only for $\epsilon_{\mu} \leq 0$. For all cases, the NMPC cost function weights are the same as in Figure 11.

In both sensitivities, the yaw rate tracking improvement brought by the preview is affected by the preview errors, but remains significant w.r.t. the configurations without preview. The rear slip angle limitation performance is more affected by the preview error on the

friction coefficient, with $\text{NMPC}_{\text{prev,}\mu\text{,20}}$ providing similar performance to $\text{NMPC}_{\text{base,20,ref}}$ for $|\epsilon_\mu| > 0.02$, but still bringing evident benefits w.r.t. $\text{NMPC}_{\text{base,20}}$.

5. Conclusions

This study evaluated the potential benefits of road preview implementations for NMPC-based ICC with TV and F2T ARMD actuations. The main conclusions are:

- Although the adoption of accurate road preview and prediction models that are well-aligned with the vehicle plant can imply longer optimal prediction horizon values (e.g. up to 300 ms in Figure 7(c)), in the presence of realistic mismatches, the best results are provided by shorter t_h values, e.g. 75 ms in Figure 7(a).
- During the considered extreme sinusoidal steering manoeuvre in constant high-friction conditions, for the nominal vehicle parametrisation, the steering angle and reference yaw rate preview of $\text{NMPC}_{\text{prev,20}}$ brings yaw rate tracking benefits, corresponding to a 72% $\dot{\psi}_{RMSE}$ reduction w.r.t. $\text{NMPC}_{\text{base,20}}$, i.e. the controller configuration without preview (see Table 2). Such benefit marginally increases to 74% for $\text{NMPC}_{\text{prev,ay,pred,20}}$, which also includes the road preview on the lateral acceleration, and thus the lateral load transfer.
- The inclusion of the actuation dynamics within the prediction model improves the yaw rate tracking performance only in the presence of preview, bringing $\dot{\psi}_{RMSE}$ reductions in the 15-to-20% range when considering the ASS dynamics only, and up to 60% when concurrently considering the ASS, friction brakes and EM dynamics (Figure 9).
- In cornering conditions with highly variable tyre-road friction profiles, both $\text{NMPC}_{\text{prev,20}}$ and $\text{NMPC}_{\text{prev,ay,pred,20}}$ generate a $\sim$25% yaw rate tracking improvement w.r.t. $\text{NMPC}_{\text{base,20}}$, also in this case with negligible benefit of the lateral acceleration preview (Figure 10 and Table 3). On the contrary, the friction coefficient preview of $\text{NMPC}_{\text{prev,}\mu\text{,20}}$ allows to achieve the lowest peak value of rear axle slip angle ($\Delta\alpha_{r,max}$), and further enhances the yaw rate tracking performance by $\sim$15%.
- In case of concurrent extreme braking/traction and cornering with tyre-road friction jumps (Figure 11), the lateral acceleration preview of $\text{NMPC}_{\text{prev,ay,pred,20}}$ reduces $\dot{\psi}_{RMSE}$ by 14% w.r.t. $\text{NMPC}_{\text{prev,20}}$. The tyre-road friction preview of $\text{NMPC}_{\text{prev,}\mu\text{,20}}$ much more effectively constrains the rear slip angles, with a 34% $\Delta\alpha_{r,max}$ decrease w.r.t. $\text{NMPC}_{\text{prev,ay,pred,20}}$, and an inevitable corresponding 6% $\dot{\psi}_{RMSE}$ increment.

As a summary, preview-based ICCs show significant promise. However, the computational loads associated with the best identified controller setups, which include the actuation dynamics in the prediction model, are very challenging in terms of real-time implementability on available control hardware. Therefore, future developments will deal with imitation learning to replace the online NMPC algorithm with a neural network and achieve similar performance while improving computational efficiency.

Disclosure statement

No potential conflict of interest was reported by the author(s).

Funding

This work was supported by the European Commission: [Grant Number 101138110 (SmartCorners project)].

ORCID

Davide Lazzarini http://orcid.org/0009-0001-8703-5040
Aldo Sorniotti http://orcid.org/0000-0002-4848-058X

References

[1] Mazzilli V, De Pinto S, Pascali L, et al. Integrated chassis control: classification, analysis, and future trends. Annu Rev Control. 2021;51:172–205. doi:10.1016/j.arcontrol.2021.01.005
[2] Camacho EF, Bordons C. Model predictive control. London: Springer; 2007.
[3] Houska B, Ferreau HJ, Diehl M. ACADO toolkit – An open-source framework for automatic control and dynamic optimization. Opt Control Appl Meth. 2011;32(3):298–312. doi:10.1002/oca.939
[4] Asperti M, Vignati M, Sabbioni E. On torque vectoring control: Review and comparison of state-of-the-art approaches. Machines. 2024;12(3):160. doi:10.3390/machines12030160
[5] Dalboni M, Tavernini D, Montanaro U, et al. Nonlinear model predictive control for integrated energy-efficient torque-vectoring and anti-roll moment distribution. IEEE/ASME Trans Mechatron. 2021;26(3):1212–1224. doi:10.1109/TMECH.2021.3073476.
[6] Asperti M, Vignati M, Sabbioni E. Torque vectoring control as an energy-efficient alternative to vehicle suspensions tuning. Energies. 2024;17(12):2903. doi:10.3390/en17122903
[7] Manca R, Castellanos Molina L, Hegde S, et al. (2023). Optimal Torque-Vectoring control strategy for energy efficiency and vehicle dynamic improvement of battery electric vehicles with multiple motors. SAE Technical Paper 2023-01-0563. doi:10.4271/2023-01-0563
[8] Wang J, Gao S, Wang K, et al. Wheel torque distribution optimization of four-wheel independent-drive electric vehicle for energy efficient driving. Control Eng Pract. 2021;110:104779. doi:10.1016/j.conengprac.2021.104779
[9] Chatzikomis C, Zanchetta M, Gruber P, et al. An energy-efficient torque-vectoring algorithm for electric vehicles with multiple motors. Mech Syst Signal Process. 2019;128:655–673. doi:10.1016/j.ymssp.2019.03.012
[10] Parra A, Tavernini D, Gruber P, et al. On nonlinear model predictive control for energy-efficient torque-vectoring. IEEE Trans Veh Technol. 2021;70(1):173–188. doi:10.1109/TVT.2020.3022022
[11] De Filippis G, Lenzo B, Sorniotti A, et al. Energy-efficient torque-vectoring control of electric vehicles with multiple drivetrains. IEEE Trans Veh Technol. 2018;67(6):4702–4715. doi:10.1109/TVT.2018.2808186.
[12] Pennycott A, De Novellis L, Sabbatini A, et al. Reducing the motor power losses of a four-wheel drive, fully electric vehicle via wheel torque allocation. Proc Inst Mech Eng Part D. 2014;228(7):830–839. doi:10.1177/0954407013516106
[13] Yu M, Evangelou SA, Dini D. Advances in active suspension systems for road vehicles. Engineering. 2024;33:160–177. doi:10.1016/j.eng.2023.06.014
[14] Guastadisegni G, De Pinto S, Cancelli D, et al. Ride analysis tools for passenger cars: Objective and subjective evaluation techniques and correlation processes – A review. Veh Syst Dyn. 2024;62(7):1876–1902. doi:10.1080/00423114.2023.2259024
[15] Cvok I, Hrgetić M, Hoić M, et al. Analytical and experimental evaluation of various active suspension alternatives for superior ride comfort and utilization of autonomous vehicles. J Auton Veh Sys. 2021;1(1):011004. doi:10.1115/1.4048584
[16] Chen X, Song H, Zhao S, et al. Ride comfort investigation of semi-active seat suspension integrated with quarter car model. Mech Ind. 2022;23(1):18. doi:10.1051/meca/2022020

[17] Hsiao CY, Wang YH. Evaluation of ride comfort for active suspension system based on self-tuning fuzzy sliding mode control. Int J Control Autom Syst. 2022;20(4):1131–1141. doi:10.1007/s12555-020-0736-7
[18] Sinasac Z. Subjective evaluation of vehicle semi-active suspension for improved ride and handling [Master's dissertation]. University of Windsor, Canada; 2021.
[19] Cheng Y, Hu R, Xu W, et al. Integrated control strategy of semi-active suspension and in-wheel motors for handling limit of electric race car. Proc Inst Mech Eng Part D. 2024;238(14):4486–4504. doi:10.1177/09544070231198280
[20] Özarslan Yatak M, Şahin F. Ride comfort-road holding trade-off improvement of full vehicle active suspension system by interval type-2 fuzzy control. Eng Sci Technol Int J. 2021;24(1):259–270. doi:10.1016/j.jestch.2020.10.0
[21] Piñón A, Favela-Contreras A, Félix-Herrán LC, et al. An ARX model-based predictive control of a semi-active vehicle suspension to improve passenger comfort and road-holding. Actuators. 2021;10(3):47. doi:10.3390/act10030047
[22] Aljarbouh A, Fayaz M. Hybrid modelling and sliding mode control of semi-active suspension systems for both ride comfort and road-holding. Symmetry (Basel). 2020;12(8):1286. doi:10.3390/sym12081286
[23] Jin X, Wang J, Sun S, et al. Design of constrained robust controller for active suspension of in-wheel-drive electric vehicles. Mathematics. 2021;9(3):249. doi:10.3390/math9030249
[24] Ricco M, Alshawi A, Gruber P, et al. Nonlinear model predictive control for yaw rate and body motion control through semi-active and active suspensions. Veh Syst Dyn. 2024;62(6):1587–1620. doi:10.1080/00423114.2023.2251615
[25] Ricco M, Gruber P, Sorniotti A, et al. On the design of yaw rate control via variable front-to-total anti-roll moment distribution. IEEE Trans Veh Technol. 2020;69(2):1388–1403. doi:10.1109/TVT.2019.2955902
[26] Ricco M, Percolla A, Rizzo GC, et al. On the model-based design of front-to-total anti-roll moment distribution controllers for yaw rate tracking. Veh Syst Dyn. 2022;60(2):569–596. doi:10.1080/00423114.2020.1825753
[27] Gerhard J, Laiou M-C, Monnigmann M, et al. Robust yaw control design with active differential and active roll control systems. IFAC Proceedings Volumes. 2005;38(1):73–78. doi:10.3182/20050703-6-CZ-1902.01900
[28] Her H, Yi K, Suh J, et al. Development of integrated control of electronic stability control,: continuous damping control, and active anti-roll bar for vehicle yaw stability. IFAC Proc Vol. 2013;46(21):83–88. doi:10.3182/20130904-4-JP-2042.00152
[29] Her H, Koh Y, Joa E, et al. An integrated control of differential braking,: front/rear traction, and active roll moment for limit handling performance. IEEE Trans Veh Technol. 2016;65(6):4288–4300. doi:10.1109/TVT.2015.2513063
[30] Lin C, Siampis E, Velenis E. Path-tracking control at the limits of handling of a prototype over-actuated autonomous vehicle. Veh Syst Dyn. 2025;63(5):853–875. doi:10.1080/00423114.2024.2361726
[31] Li B, Lin C, Ahmadi J, et al. An integrated path-tracking and control allocation method for autonomous racing electric vehicles. Veh Syst Dyn. 2024;62(6):1517–1540. doi:10.1080/00423114.2023.2242533
[32] Lin C, Li B, Siampis E, et al. Predictive path-tracking control of an autonomous electric vehicle with various multi-actuation topologies. Sensors. 2024;24(5):1566. doi:10.3390/s24051566
[33] Stano P, Montanaro U, Tavernini D, et al. Model predictive path tracking control for automated road vehicles: A review. Annu Rev Control. 2023;55:194–236. doi:10.1016/j.arcontrol.2022.11.001
[34] So KM, Tavolo G, Tavernini D, et al. (2022). Novel pre-emptive control solutions for V2X connected electric vehicles. Transport Research Arena (TRA) Conference, Lisbon, Portugal. arXiv. doi:10.48550/arXiv.2406.02211
[35] Theunissen J, Tota A, Gruber P, et al. Preview-based techniques for vehicle suspension control: A state-of-the-art review. Annu Rev Control. 2021;51:206–235. doi:10.1016/j.arcontrol.2021.03.010

[36] Tavolo G, So KM, Tavernini D, et al. On antilock braking systems with road preview through nonlinear model predictive control. IEEE Trans Ind Electron. 2024;71(8):9436–9448. doi:10.1109/TIE.2023.3314917
[37] Tavolo G, So KM, Tavernini D, et al. (2022). Nonlinear model predictive control for preview-based traction control. The 15th International Symposium on Advanced Vehicle Control (AVEC), 1–6. doi:10.48550/arXiv.2406.02206
[38] Scamarcio A, Caponio C, Mihalkov M, et al. Predictive anti-jerk and traction control for V2X connected electric vehicles with central motor and open differential. IEEE Trans Veh Technol. 2023;72(6):7221–7239. doi:10.1109/TVT.2022.3143497
[39] Parra A, Tavernini D, Gruber P, et al. On pre-emptive vehicle stability control. Veh Syst Dyn. 2022;60(6):2098–2123. doi:10.1080/00423114.2021.1895229.
[40] Yim S. Design of a preview controller for vehicle rollover prevention. IEEE Trans Veh Technol. 2011;60(9):4217–4226. doi:10.1109/TVT.2011.2169687
[41] Yim S. Preview controller design for vehicle stability with V2V communication. IEEE Trans Intell Transp Syst. 2016;18(6):1–10. doi:10.1109/TITS.2016.2607283
[42] Amer NH, Dalboni M, Georgiev P, et al. Integrated torque-vectoring and anti-roll moment distribution strategies based on optimal control: Influence of model complexity and road curvature preview. Veh Syst Dyn. 2024;62(10):2533–2566. doi:10.1080/00423114.2023.2296586
[43] Peenze AJ, Els PS. Investigation of steer preview methods to improve predictive control methods on off-road vehicles with realistic actuator delays. J Terramech. 2025;117:101027. doi:10.1016/j.jterra.2024.101027
[44] Dai C, Zong C, Chen G. Path tracking control based on model predictive control with adaptive preview characteristics and speed-assisted constraint. IEEE Access. 2020;8:184697–184709. doi:10.1109/ACCESS.2020.3029635
[45] Ahn T, Lee Y, Park K. Design of integrated autonomous driving control system that incorporates chassis controllers for improving path tracking performance and vehicle stability. Electronics (Basel). 2021;10(2):144. doi:10.3390/electronics10020144
[46] Zhai L, Wang C, Hou Y, et al. MPC-based integrated control of trajectory tracking and handling stability for intelligent driving vehicle driven by four hub motors. IEEE Trans Veh Technol. 2022;71(3):2668–2680. doi:10.1109/TVT.2022.3140240
[47] https://www.avl.com/en/simulation-solutions/software-offering/simulation-tools-a-z/avl-vsm. [last accessed on 2025 Dec 14].
[48] Pacejka H. Tire and vehicle dynamics. Amsterdam: Elsevier; 2005.
[49] Genta G. Motor vehicle dynamics: modeling and simulation. Singapore: World Scientific; 1997.
[50] Kerrigan EC, Maciejowski JM. (2000). Soft constraints and exact penalty functions in model predictive control. Control 2000 Conference: Cambridge, 2319–2327.
[51] Li A, Jiang H, Zhou J, et al. Implementation of human-like driver model based on recurrent neural networks. IEEE Access. 2019;7:98094–98106. doi:10.1109/ACCESS.2019.2930873